

# A Study of the Response of the OPAL Calorimeter to Hadrons

by

Ping Hu

B.Sc., Beijing Normal University, 1983

A thesis submitted in partial fulfilment  
of the requirements for the degree of

MASTER OF SCIENCE

in the Department  
of Physics and Astronomy.

We accept this thesis as conforming  
to the required standard.

---

Dr. R.K.Keeler, Supervisor (Department of Physics and Astronomy)

---

Dr. A.Astbury, Departmental Member (Department of Physics and Astronomy)

---

Dr. D.Hoffman, Outside Member (Department of Computer Science)

---

Dr. C.J.Oram, External Examiner (TRIUMF Laboratory)

© Ping Hu, 1995,  
University of Victoria.

All rights reserved. Thesis may not be reproduced in whole or in part,  
by mimeograph or other means, without the permission of the author.

Supervisor: Dr. R.K.Keeler

### ABSTRACT

The response of the OPAL calorimeters to hadrons is analysed using single charged pions from tau decays. The sample is over 98% pure and momentum analyzed. A calibration correction for the hadron calorimeter is given. The electromagnetic calorimeter energy weighting for the hadrons is optimized. The precision of the energy measurement of the hadron calorimeter with and without the electromagnetic calorimeter are studied. Results are compared with the Monte Carlo simulation. The measured energy resolution of the hadron calorimeter can be expressed as:

$$\frac{\sigma_{HC_{data}}}{E} = (20.1 \pm 2.6)\% + \frac{(62.8 \pm 11.5)\%}{\sqrt{E}}$$

Examiners:

---

Dr. R.K.Keeler, Supervisor (Department of Physics and Astronomy)

---

Dr. A.Astbury, Departmental Member (Department of Physics and Astronomy)

---

Dr. D.Hoffman, Outside Member (Department of Computer Science)

---

Dr. C.J.Oram, External Examiner (TRIUMF Laboratory)

## **Acknowledgements**

This thesis would not have been possible without the help of a number of people. I would like to thank Richard Keeler for his advice and guidance. I wish to express my sincere gratitude to Myron Rosvick and Paul Poffenberger for their help, support and encouragement with the analysis and writeup. I would also like to thank Randy Sobie for his critical reading and useful comments of this thesis. Finally, I would like to thank Ian Lawson for his patience while answering my questions, and Johannes Steuerer for careful reading of early versions of this thesis.

# Contents

<b>Abstract</b>	<b>ii</b>
<b>Acknowledgements</b>	<b>iii</b>
<b>1 Introduction</b>	<b>1</b>
<b>2 Physics with OPAL and LEP</b>	<b>3</b>
2.1 Physics at an $e^+e^-$ collider . . . . .	3
2.1.1 The OPAL Detector . . . . .	4
2.1.2 Calorimeter . . . . .	5
<b>3 Particle Interactions with Matter</b>	<b>10</b>
3.1 Electromagnetic absorption . . . . .	10
3.1.1 Ionization . . . . .	10
3.1.2 Electron and photon showers . . . . .	11
3.2 Nuclear Interactions . . . . .	13
3.2.1 The hadronic shower . . . . .	13
3.3 Expected Energy Response and Resolution . . . . .	16
<b>4 Data Selection</b>	<b>18</b>
4.1 The experimental data and the Monte Carlo samples . . . . .	18
4.2 Selection of tau pair events . . . . .	19
4.3 Selection of Pions . . . . .	21
4.4 Selection of muons . . . . .	24
4.5 Pion Shower Profile . . . . .	26

<b>5</b>	<b>Intrinsic Energy Resolution</b>	<b>29</b>
5.1	Energy Calibration and Corrections . . . . .	29
5.2	The HCAL Energy Resolution . . . . .	36
<b>6</b>	<b>Combined Energy Resolution</b>	<b>40</b>
6.1	ECAL Energy weighting . . . . .	40
6.2	The Hadronic Energy Resolution with the Combined Calorimeter . . . . .	44
<b>7</b>	<b>Conclusions and Discussion</b>	<b>49</b>
<b>A</b>	<b>The Treatment of Measurements Within Wide Bins</b>	<b>51</b>

# List of Tables

2.1	The branching ratios of the most common single charged particle decay modes. . . . .	4
5.1	Fitting parameters of $E_{HC} - (p_{trk} - \Delta E_{mi})$ for data and MC. . . . .	34
5.2	Polynomial correction parameters of HCAL energy for data and MC. . . . .	35
6.1	The $\alpha$ for six momentum bins . . . . .	42
6.2	Polynomial parameters of $\alpha$ as a function of momentum for data and MC. . . . .	43
6.3	Fitting parameters of $\alpha E_{EC} + E_{HCcor} - p_{trk}$ for data and MC. . . . .	47

# List of Figures

2.1	Born level Feynman diagram. . . . .	4
2.2	The OPAL detector. . . . .	6
2.3	The configuration of the barrel HCAL . . . . .	8
3.1	A typical plot of energy loss versus momentum. . . . .	12
4.1	The pion candidates momentum distributions after initial rejection. . . . .	22
4.2	The momentum distributions for the tau pair sample and the single pion candidate . . . . .	25
4.3	The ECAL energy distributions for minimum EM-interacting pions and muons . . . . .	26
4.4	The profile of hadronic shower . . . . .	27
5.1	The plot shows the energy loss by ionization. . . . .	30
5.2	The difference between the measured and expected HCAL energy versus the incident energy. . . . .	31
5.3	$E_{HC} - (p_{trk} - \Delta E_{mi})$ spectrum for data . . . . .	32
5.4	$E_{HC} - (p_{trk} - \Delta E_{mi})$ spectrum for MC. . . . .	33
5.5	HCAL energy calibration correction . . . . .	35
5.6	The distributions of $E_{HCcor} - (p_{trk} - \Delta E_{mi})$ . . . . .	36
5.7	The HCAL energy resolution for pion data and MC simulations . . . . .	38
6.1	The $\chi$ distribution for two formulae . . . . .	42
6.2	The ECAL weight, $\alpha$ , as a function of incident momentum . . . . .	43
6.3	$\alpha E_{EC} + E_{HCcor} - p$ spectrum for data. . . . .	45

6.4	$\alpha E_{EC} + E_{HCcor} - p_{trk}$ spectrum for MC . . . . .	46
6.5	The combined energy resolution . . . . .	48



# Chapter 1

## Introduction

The OPAL (Omni Purpose Apparatus at LEP) detector [1] is one of four operating at the LEP (Large Electron Positron) [2] collider at CERN. The detector is designed to make precision tests of the Standard Model [3] of particle physics and to search for new particles and rare processes. It does this by measuring the kinematics (*i.e.* energy, vector momentum and velocity) of each particle generated in the  $e^+e^-$  collisions. The types of particles observed with the detector fall into three categories depending on how they interact with matter: through ionization only, by producing electromagnetic showers or by producing hadronic showers.

The OPAL detector consists of several subdetectors. A more detailed discussion of the detector is given in chapter 2. The subdetectors that measure energy, called calorimeters, are the subject of this thesis. The OPAL calorimeters are divided into two parts. The first is the electromagnetic calorimeter, which absorbs the total energy of particles that interact with matter by making electromagnetic showers. The second, or hadron calorimeter, adds the extra material required to totally absorb a particle that produces hadronic showers. Particles with this property are known as hadrons.

In this thesis the response of the hadron calorimeter to hadrons is analysed. The calibration of the hadron calorimeter is studied and the energy resolution of the OPAL calorimeters for hadrons is measured. A sample of hadrons is selected from the OPAL data

using the special properties of tau particles produced in the reaction  $e^+e^- \rightarrow Z^0 \rightarrow \tau^+\tau^-$ . The theoretical basis of the production of tau leptons and their subsequent decay to hadrons is described in chapter 2. The selection produces a very pure set of events that consist of a single charged pion resulting from  $\tau^- \rightarrow \pi^- \nu_\tau$  decays<sup>1</sup>. The pions are momentum analyzed in the OPAL detector. The energy measurement in the calorimeter can therefore be compared to a known momentum.

The interaction of particles with matter is discussed in chapter 3. In particular the expected response of the calorimeters to hadrons is described. Chapter 4 explains the details of how a pure sample of single isolated pions is selected from the data collected by the OPAL experiment. The purity of the selection is calculated. The data are compared to the expected momenta for the particles and are shown to be consistent with expectations. A subsample of pions that do not shower in the electromagnetic calorimeter is selected and discussed.

Chapter 5 uses the sample of pions that do not shower in the electromagnetic calorimeter to calibrate the hadron calorimeter energy against the measured momentum of the pion and to measure the intrinsic resolution of the hadron calorimeter. The total sample of pions is used in chapter 6 to optimize the energy weighting used when the measured energies in the electromagnetic and hadronic calorimeters are added together. The results of the analyses are discussed in chapter 7.

---

<sup>1</sup>The charge conjugate decay is assumed to be included throughout the rest of this thesis.

# Chapter 2

## Physics with OPAL and LEP

### 2.1 Physics at an $e^+e^-$ collider

The LEP collider is an  $e^+e^-$  storage ring with a circumference of 27 km [2], located at the CERN laboratory in Geneva, Switzerland. There are eight interaction zones in the LEP accelerator ring. Four of these zones are occupied by large detectors: OPAL [1], ALEPH [4], DELPHI [5], and L3 [6]. The data described here were taken by the OPAL experiment during the years 1991 to 1994.

In the interaction zones of the LEP collider, electrons and positrons collide and annihilate to fermion-antifermion pairs. The annihilation process can be described to lowest order as a weak neutral current interaction or as an electromagnetic interaction, depending upon the collision energy. The centre-of-mass energy of LEP is approximately 91 GeV, corresponding to the peak of the  $Z^0$  mass resonance. The  $Z^0$  is the exchange particle responsible for the neutral weak interaction. The dominant process at LEP is  $e^+e^- \rightarrow Z^0 \rightarrow f\bar{f}$ . Fig. 2.1(a) shows the Born level Feynman diagram representing the amplitude for the  $\tau^+\tau^-$  final state which is used in this thesis. The  $\tau$  is a charged lepton with a mass of  $1777.1 \text{ MeV}/c^2$  [7]. It is heavier than some of the light mesons, in particular the pion ( $\pi$ ,  $140 \text{ MeV}/c^2$ ), kaon ( $K$ ,  $494 \text{ MeV}/c^2$ ), and rho ( $\rho$ ,  $770 \text{ MeV}/c^2$ ), and can therefore decay not only into lighter leptons, but also into hadrons. Both the hadronic and the semileptonic decays of the  $\tau$  involve the charged weak force. The branching ratios of

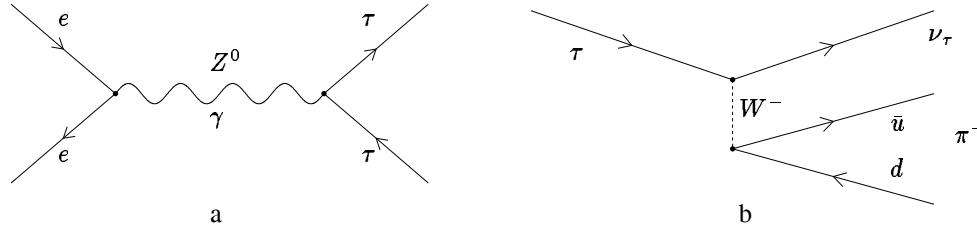


Figure 2.1: (a) Feynman diagram depicting the annihilation of an  $e^+e^-$  pair to form a  $Z^0$  or  $\gamma$  which then decays to a  $\tau^+\tau^-$  pair. (b) Feynman diagram depicting  $\tau^- \rightarrow \pi^- \nu_\tau$  decay.

decay modes	BR %
$\tau^- \rightarrow \rho^- \nu_\tau$	$25.2 \pm 0.4$
$\tau^- \rightarrow e^- \bar{\nu}_e \nu_\tau$	$18.01 \pm 0.18$
$\tau^- \rightarrow \mu^- \bar{\nu}_\mu \nu_\tau$	$17.65 \pm 0.24$
$\tau^- \rightarrow \pi^- \nu_\tau$	$11.7 \pm 0.4$
$\tau^- \rightarrow h^- 2\pi^0 \nu_\tau$	$9.6 \pm 0.4$
$\tau^- \rightarrow K^- \nu_\tau$	$0.67 \pm 0.23$

Table 2.1: The branching ratios of the most common one charged particle decay modes. The symbol  $h^-$  represents  $\pi^-$ 's and  $K^-$ 's.

the most common decay modes of the  $\tau$  with one charged particle in the final state [7] are given in table 2.1.

In this thesis the  $\pi^-$  from  $\tau^- \rightarrow \pi^- \nu_\tau$  decays are selected. However, we consider both  $\pi^- \nu_\tau$  and  $K^- \nu_\tau$  decays together since they have similar interactions in the calorimeter. The Born level Feynman diagram depicting the  $\tau^- \rightarrow \pi^- \nu_\tau$  decay is shown in Fig. 2.1(b).

### 2.1.1 The OPAL Detector

The OPAL detector has been fully described in reference [1]. A summary of the aspects relevant to this thesis is given here. The general layout of the the detector is shown in Fig. 2.2, which indicates the location and relative sizes of the various subdetector components.

The OPAL coordinate system is a right-handed orthonormal system with its origin at the nominal interaction point at the centre of the detector.  $z$  is along the  $e^-$  beam direction,  $\phi$  is the azimuthal angle and  $\theta$  is the polar angle with respect to  $z$ .

*The central tracking chambers* are located at the centre of the detector inside a solenoid which provides a uniform magnetic field of 0.435 T aligned with the incoming electron beam. The tracking chambers are used to measure the momenta of charged particles by detecting the curvature of the particle trajectories in the magnetic field. Track position and energy loss are measured at the same time. The central tracking chambers consists of three parts: a vertex detector (CV), a jet chamber (CJ) and z-chambers. The momentum resolution in the direction transverse to beams is given by [8]

$$\sigma_{p_T}/p_T = \sqrt{(0.02)^2 + (0.0015p_T)^2}. \quad (2.1)$$

The solenoidal coil is surrounded by a scintillation counter array which measures the time of flight of particles relative to the beam interaction time. It is useful for excluding particles that do not come from the interaction region.

### 2.1.2 Calorimeter

Outside of the time-of-flight scintillation counters are the calorimeters which absorb the energy of the incoming particles. These are the electromagnetic calorimeter and the hadronic calorimeter.

The first layer is called *the electromagnetic calorimeter* (ECAL). It is optimized to measure the energies and positions of electrons, positrons and photons. Hadrons may also start to form hadronic showers in the ECAL. These showers are only partially contained in this detector. The electromagnetic calorimeter consists of two parts: a system of preshower counters (presampler) followed by a lead glass calorimeter. The material in front of the calorimeter, mostly due to the solenoid and central detector pressure vessel, causes most electromagnetic showers to begin before reaching the lead glass. The

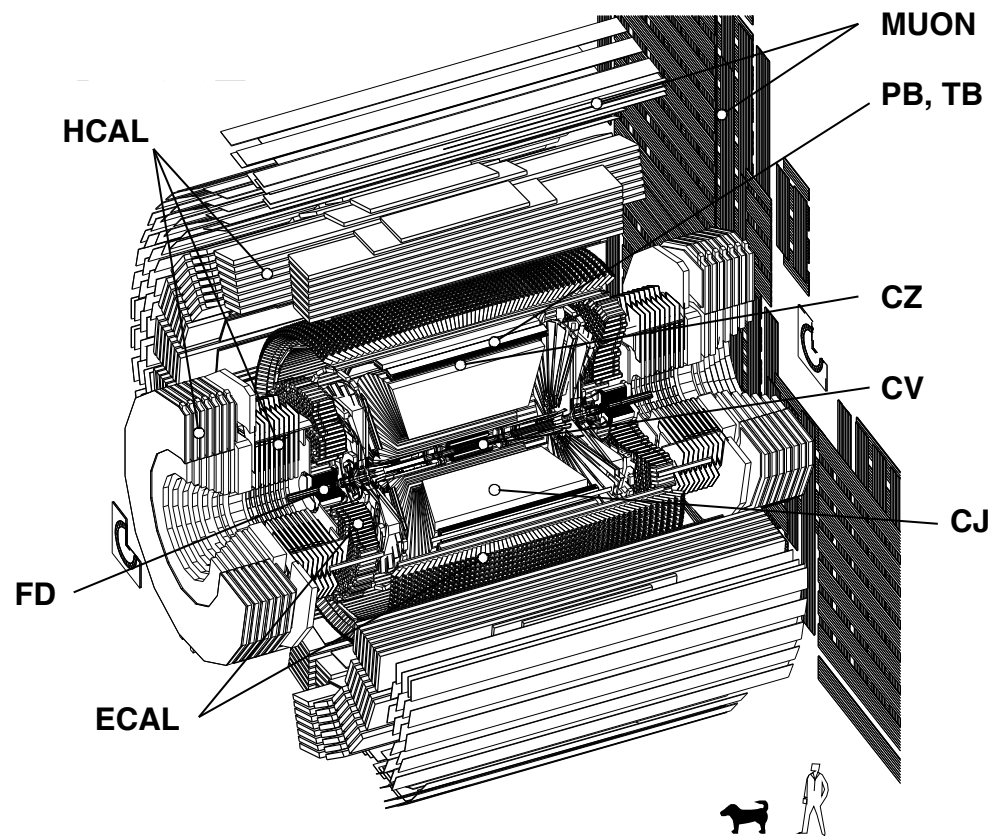


Figure 2.2: The OPAL detector. HCAL: hadron calorimeter, ECAL: electromagnetic calorimeter, MUON: muon chamber, PB: barrel presampler, TB: time-of-flight (in barrel region), CV: vertex detector, CJ: jet chamber, CZ:  $z$ -chamber, FD: forward detector.

presampler is therefore installed to measure the amount of shower development before the lead glass. The lead glass calorimeter is divided into a barrel (EB) ( $|\cos \theta| < 0.81$ ), and two endcaps (EE) ( $0.81 < |\cos \theta| < 0.91$ ). The barrel part consists of 9440 lead-glass blocks  $10\text{ cm} \times 10\text{ cm}$  wide and 24.6 radiation lengths deep, pointing toward the beam interaction region. In the endcap there are 2264 lead-glass blocks aligned parallel to the beam pipe.

### Hadron calorimeter at OPAL

The hadron calorimeter measures the energy after a particle has passed through the ECAL. The detector consists of three parts: the barrel,  $|\cos \theta| < 0.81$ , the endcaps,  $0.81 < |\cos \theta| < 0.91$ , and the pole tips,  $0.91 < |\cos \theta| < 0.99$ . The entire hadron calorimeter has a coverage of about 97% of the solid angle. The barrel part of the hadron calorimeter will be considered in this analysis. It covers about 80% of the total solid angle in the central region of the detector [9].

The barrel hadron calorimeter (see Fig. 2.3(a)) is a sampling calorimeter which uses the iron of the magnetic flux return yoke as the absorbing material. The barrel spans radii from 3.4 m to 4.4 m from the beam line and contains more than 4 interaction lengths of iron absorber. The iron is divided into eight 100 mm thick plates, and interleaved with nine 25 mm thick layers of plastic streamer tubes which form the active elements of the calorimeter (see Fig. 2.3(b)). The barrel detector is divided into 24 wedge-shaped segments in  $\phi$ , with most segments extending the full length (10.4 m) of the barrel. Two pairs of segments, at the top and the bottom of the detector, are shortened to provide space for the muon chamber support structure.

Each streamer tube layer consists of a series of chambers (see Fig. 2.3(c)), with each chamber containing 7 or 8 cells, depending upon the width of that layer. Each chamber is contained within a gas envelope which is filled with a mixture of 75% isobutane and 25%

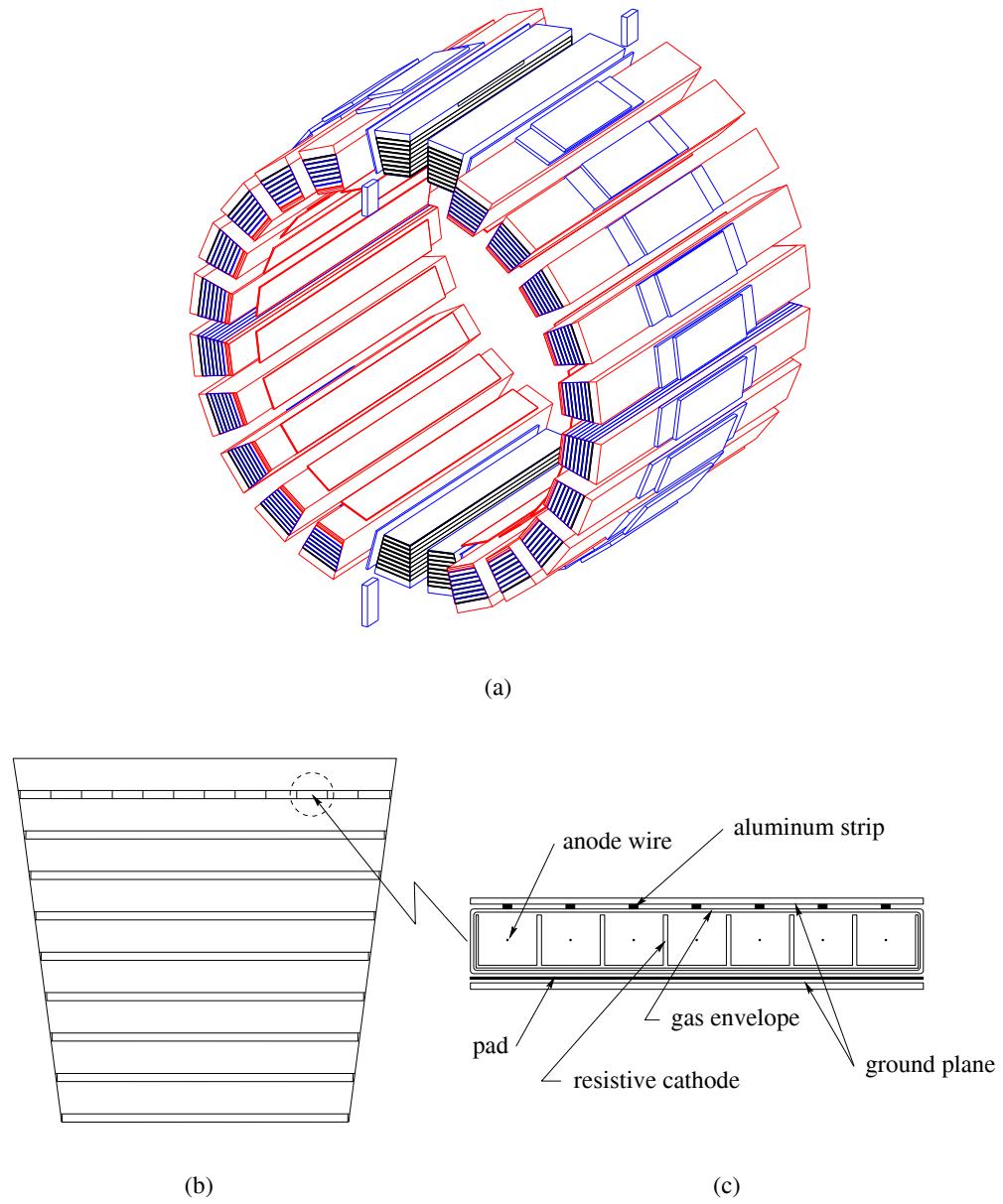


Figure 2.3: Figure (a) shows the HCAL barrel; Figure (b) shows the cross-section of one of the barrel wedges; Figure (c) shows the cross-section of one of the chambers in a layer.



argon. Each cell has three cathode walls and an anode wire in the centre. Layers 2 through 8 consist of two half-length ( $\sim 5\text{ m}$ ) chambers with a junction between the layers near  $\cos\theta = 0$ . The junctions are staggered from layer to layer to avoid gaps in the acceptance of the detector. The first and last layers are single  $7.3\text{ m}$  long chambers.

The signals are read out on both the upper and lower faces of the chambers. In the chambers the pulses are induced through the grounded cathode and the gas envelope to the pads under the chambers and to the  $4\text{ mm}$  wide aluminum strips above the anode wire in each cell (see Fig. 2.3(c)). The strips (HS) are read out at either end of the gas envelope, providing approximately 58,000 individual digital signals. These signals provide precise single particle tracking for muon detection, and are useful in profiling the shape of the hadronic shower. The layers of pads are grouped together to form a matrix of  $105\text{ mrad} \times 105\text{ mrad}$  towers [10] pointing towards the interaction region. Unit gain summing amplifiers are used to sum the signals from the pads in each tower to provide an estimate of the energy in the hadronic showers.

Essentially all the hadrons produced in LEP collisions are absorbed by the hadron calorimeter, leaving only muons to pass into the surrounding *Muon Detector*. The muon detector consists of four layers of drift chambers in barrel (MB) and endcaps, covering 93% of the solid angle.

# Chapter 3

## Particle Interactions with Matter

When an interacting particle passes through matter, it loses energy through a number of processes. The interactions cause the excitation and ionization of the atoms in the material. This energy is eventually dissipated as heat. Hence particle detectors that measure the energy deposited by totally absorbed particles are known as calorimeters. The processes involved include electromagnetic interactions, nuclear interactions and weak interactions, depending upon the energy and type of incident particle. Section 3.1 discusses the electromagnetic interaction processes, and section 3.2 discusses the nuclear interaction processes. Section 3.3 discusses the energy response and resolution of calorimeters.

### 3.1 Electromagnetic absorption

There are two electromagnetic phenomena that are important for particle detection: ionization loss and shower development. Many detectors are based on the principle of charged particles ionizing a medium.

#### 3.1.1 Ionization

The important energy loss mechanism for heavy charged particles (*eg.*  $\pi^\pm$ ,  $p$ ) is through collisions with the atomic electrons of the medium. The atomic electrons can be either lifted to higher energy levels, called excitation, or ejected from the atom, called ionization.

Energy loss by ionization is given by the Bethe-Bloch formula [7], which approximates the average energy deposition per unit path length ( $dE/dx$ ) in terms of the particle energy:

$$-\frac{dE}{dx} = \frac{4\pi n z^2 e^4}{m_e v^2} \left[ \ln \left( \frac{2m_e v^2}{I(1-\beta^2)} \right) - \beta^2 - \frac{\delta}{2} \right]. \quad (3.1)$$

In this formula  $m_e$  is the electron mass,  $z$  and  $v$  are the charge and the velocity of the particle,  $\beta = v/c$ ,  $n$  is the number of electrons per  $\text{cm}^3$  in the medium,  $E$  is the energy in MeV,  $x$  is the path length measured in  $\text{g cm}^{-2}$ ,  $I$  is the mean excitation energy which is approximately  $10 \text{ eV}$  for absorber materials with  $Z > 8$  [7] and  $\delta$  is the density correction factor.

A plot of the energy loss as a function of momentum is shown in Fig. 3.1. The energy loss drops rapidly with increasing velocity of the particle, until an *ionization minimum* occurs at about  $\beta = 0.95$ , then it starts to increase slowly because of relativistic effects (*relativistic rise*). At high momenta the energy loss saturates at what is known as the *Fermi plateau*.

### 3.1.2 Electron and photon showers

At high energies, photons are produced by light charged particles such as electrons and positrons by bremsstrahlung. Subsequently the photons interact with the detector material by producing electron-positron pairs if the photon has sufficient energy. The newly formed electrons and positrons also lose their energy by bremsstrahlung, producing photons which continue to undergo further pair production if they are of high enough energy. The energy of the incident particles is split between the photons and the electrons and positrons. The resulting cascade of electrons and photons is known as an electromagnetic shower. While the electromagnetic (EM) shower is developing, the number of particles is increasing and the lateral dimensions are also increasing due to multiple scattering processes. At the same time, the average energy of the particles in the shower is decreasing, until it falls

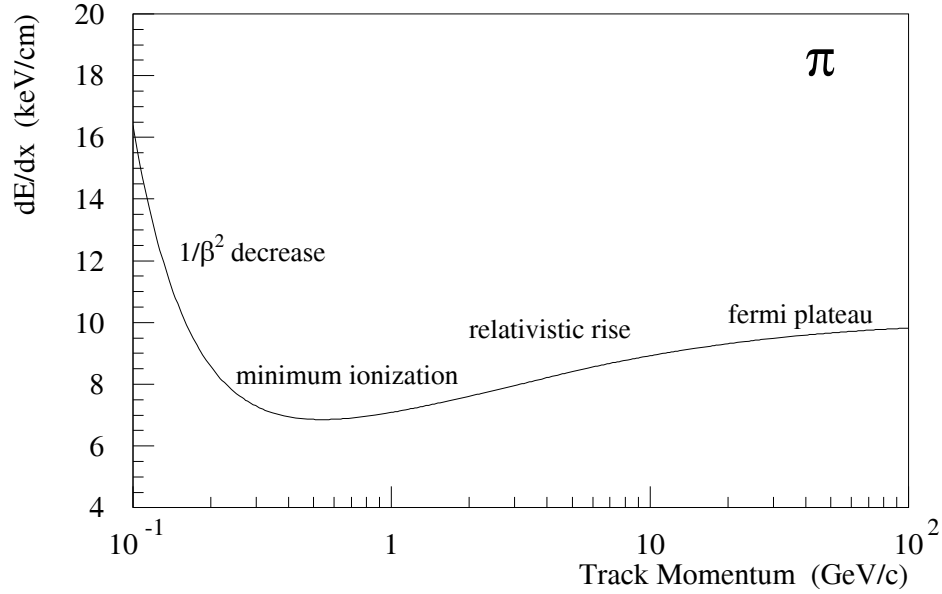


Figure 3.1: A typical plot of energy loss,  $dE/dx$ , versus momentum.

below the critical energy  $E_c$  ( $E_c \approx 600/Z \text{ MeV}$  [11]), where the particle multiplication stops because loss of energy by ionization becomes more important than bremsstrahlung.

The mean distance an electron travels in matter before emitting bremsstrahlung is called the *radiation length* and is denoted by  $X_0$ . It determines the longitudinal development of an electromagnetic shower in matter and can be approximated by [12],

$$X_0 \simeq 180 A/Z^2 \text{ gcm}^{-2} \quad (3.2)$$

At low energies (about  $E_c$ ), photons interact mainly through Compton scattering and the photoelectric effect. Low energy electrons, which are produced from Compton scattering and the photoelectric effect at the end of a EM shower, lose their energy through ionization.

## 3.2 Nuclear Interactions

Nuclear interactions between a particle and matter are more complicated than electromagnetic interactions. There are a large number of different nuclear processes which a particle may undergo. Because of this complexity, the Monte Carlo method is useful to obtain predictions of the interactions on a statistical basis. Here only the elementary physics processes are discussed.

An energetic hadron can lose energy in matter by elastic and inelastic scattering with the nuclei of the medium. In an elastic scattering process the energy of the incident particle changes due to the recoil of the scattering nucleus in the medium, but the nuclear state of the particle remains unchanged. The fraction  $f$  of the incident particle energy transferred to the medium is given by [13]

$$f = \frac{1}{A + 1}, \quad (3.3)$$

where  $A$  is the nuclear mass of the medium. Therefore, if the nuclei in the material are light, the recoil energy becomes an important factor.

In inelastic scattering, the particles become excited, break up, or even produce other particles. These may in turn lose their kinetic energy by ionization or induce new reactions, continuing the process of hadronic shower development.

### 3.2.1 The hadronic shower

When a high-energy hadron scatters from an atomic nucleus in a medium, spallation will occur. Spallation contains two steps [13]:

1. Intranuclear cascade. An incoming particle interacts with a nucleon inside the nucleus. It may transfer enough energy to the nucleon to move it within the nucleus and cause it to hit other nucleons. This results in the development of an intranuclear cascade. In this process pions or other mesons are often produced, and some of the

faster nucleons ( $p, n$ ) are emitted with enough energy to cause further intranuclear cascades in other nuclei.

2. Evaporation. The highly excited nucleus remaining from each intranuclear cascade decays by liberating neutrons and possibly other nucleons until the excitation energy is smaller than the binding energy (a few MeV) of the nucleon. Subsequently it decays by emitting  $\gamma$ -rays.

Highly excited nuclei can be created by spallation or by fast neutrons. If a highly excited nucleus has a large  $Z$ , where  $Z$  is the charge of the nucleus in multiples of the elementary charge  $e$ , then it may decay by fission. Fission describes the breakdown of the nuclei into two approximately equal fragments and a number of slow neutrons. Fission is usually accompanied by the emission of photons which are produced when the initial fission fragments decay to ground states.

A hadronic shower develops in matter via the processes described above. It is characterized by multiparticle production and particle emission by excited nuclei.

Neutral pions are often produced as secondary mesons in inelastic collisions and charge exchange interactions by charged pions. They decay into two photons with a branching ratio of about 99%. The photons initiate electromagnetic showers. Therefore, hadronic showers contain an electromagnetic component that is generated at the particle level. The effect causes a large variation in the response of calorimeters to hadrons depending on how much of the incident hadron energy is converted into electromagnetic shower energy.

The typical hadronic shower dimensions scale with the nuclear interaction length  $\lambda$ . It is the mean free path length of a particle before undergoing inelastic nuclear scattering. It can be approximated by [12]

$$\lambda \simeq 35 A^{1/3} g cm^{-2} \quad (3.4)$$

Hadronic showers differ from electromagnetic showers by their longer longitudinal dimension. The effect can be seen by comparing the nuclear absorption length  $\lambda$ , which is proportional to  $A^{1/3}$ , with the radiation length  $X_0$ , which is proportional to  $A/Z^2$ . Another important characteristic for hadronic showers is that about half of the incoming hadron energy is given to fast secondaries. The average transverse momentum of the secondary hadron is about 350 MeV/c [15]. Therefore the hadronic shower is also more spread out than the electromagnetic one. In addition a hadronic shower can start much deeper in the medium than an electromagnetic shower.

### **Invisible energy**

In the development of hadronic showers, a certain fraction of the energy remains undetected. For example, when slow neutrons are created by nuclear evaporation, a sizeable amount of the available energy is used to liberate the nucleons from the field that binds the nucleus. Such energy is not detected by the calorimeter. This effect is called *binding energy loss*. Some fraction of this binding energy loss may be recovered when neutrons are captured by other nuclei.

Another contribution to the undetectable energy results from slow charged pions, which were produced in the nuclear reaction. The low-energy charged pions decay into  $\mu$  and  $\nu_\mu$  via the weak interaction. The  $\nu_\mu$  escapes from the calorimeter. The  $\mu$  only ionizes minimally and nearly always escapes due to its long lifetime of 2.2  $\mu s$ .

Furthermore, the ionization from the slow nuclear fragments is usually dense and can saturate the active medium, and thus does not contribute efficiently to the energy measurement in the calorimeter.

### 3.3 Expected Energy Response and Resolution

The energy resolution is the precision of the energy measurement in the calorimeter. In general the energy resolution of a hadronic calorimeter is limited by four features:

1. There are *intrinsic fluctuations* from event to event in the fraction of the initial energy that is transformed into the visible energy in the shower (see section 3.2.1) which come from the statistics of the elementary physical processes. These fluctuations degrade the energy resolution of any hadronic calorimeter.
2. There are the fluctuations in the amount of energy deposited in the active layers. These are called *sampling fluctuations* which depend on the fraction of the initial energy deposited in the active material.
3. *Detector imperfections, intercalibration errors and shower leakage* degrade the energy resolution as well.
4. The calorimeter response to the electromagnetic part ( $e$ ) of a hadron shower is generally greater than the response to the non-electromagnetic part ( $h$ ) at the same energy because of invisible energy loss in the hadronic shower. The ratio of  $e/h$  also depends on the fraction of the EM component in the hadronic shower. So the fluctuations in the fraction of the EM component and the deviation of  $e/h$  from one, (called noncompensation) will contribute to the degradation of the energy resolution [13].

The nature of the sampling fluctuation and the intrinsic shower fluctuation are purely statistical, and are therefore proportional to the number ( $n$ ) of particles passing an active layer, where  $n$  has a Poisson distribution with variance  $\sqrt{n}$ . In linear calorimeters the measured energy of a shower is directly proportional to  $n$ . Therefore the sampling fluctuation and the intrinsic shower fluctuation contribute to the energy resolution of the



calorimeter according to:

$$\sigma_{hc}(E)/E \propto c/\sqrt{E} \quad (3.5)$$

The detector imperfections and noncompensation contribute a constant term to the energy resolution of the calorimeter. The total energy resolution of a hadronic calorimeter is conveniently expressed as [14]  $\sigma_{hc}/E = a \oplus b/\sqrt{E}$ . It is generally found, and previously used in OPAL, that

$$\sigma_{hc}/E = a + \frac{b}{\sqrt{E}} \quad (3.6)$$

fits better. A comparison between the data and the two parametrizations will be discussed later in the thesis.

# Chapter 4

## Data Selection

The analysis presented in this thesis is based on  $e^+e^- \rightarrow Z^0 \rightarrow \tau^+\tau^-$  events. The data selection is discussed in this chapter. First, the experimental data and the Monte Carlo (MC) samples are outlined. Next, the standard tau-pair event selection of the OPAL collaboration is described. The selection of charged pions and muons from tau-decays is discussed in sections 4.3 and 4.4. The final section presents the hadronic shower profile for the selected events.

### 4.1 The experimental data and the Monte Carlo samples

The experimental data used in this analysis were collected using the OPAL detector from 1991 - 1994. The detector provides raw data which are processed through an event reconstruction program (ROPE) [16]. These events are then passed through the event selection algorithm described below.

The data considered for this analysis must meet the following subdetector requirements:

	CV	CJ	TB	PB	EB	EE	HS	MB
Detector	3	3	3	3	3	3	3	3
Trigger	-	2	-	-	2	3	-	-

The subdetector [1] status words are defined as follows: 0 indicates that subdetector status is unknown; 1 indicates that subdetector is off; 2 indicates that subdetector is partially on;

3 indicates that subdetector is fully on.

Monte Carlo simulations were used to estimate efficiencies and the purity of the event selection algorithm. Monte Carlo uses random sampling methods to model statistical processes.

In this analysis, four-vector momenta  $(E, p_x, p_y, p_z)$  of 162,869 simulated tau-pair events are created by the KORALZ3.8 [17] event generator. The four-vectors are passed through program GOPAL [18] which simulates the passage of particles through the OPAL detector. GOPAL produces output in the same format as real data taken using the OPAL detector. The event reconstruction code (ROPE) and event selection program are then run on the Monte Carlo simulated data. Data and Monte Carlo simulation are compared in the analysis.

## 4.2 Selection of tau pair events

Tau pair events are selected using the OPAL tau working group procedure [21, 22]. It is briefly described in this section.

Tau pair events are selected via a two-step process. First  $e^+e^- \rightarrow Z^0 \rightarrow \ell^+\ell^-$  events are selected by considering only good charged tracks and good electromagnetic clusters in the candidate events, and by removing the non-lepton pairs through cuts. A lepton pair event must have exactly two jets<sup>1</sup> and each jet must contain at least one charged track. Non-lepton pair events, such as quark-antiquark ( $q\bar{q}$ ), or ‘multihadron’ events, two photon events, or cosmic rays, are rejected with the following cuts.

- Good charged track definition:

$$N_{CJ}^{hit} \geq 20 \quad \text{number of hits in the jet chamber.}$$

$$p_t \geq 0.1 \text{ GeV} \quad \text{momentum transverse to the beam direction.}$$

---

<sup>1</sup>A jet is defined in terms of the tracks and clusters in the event [19]. It is a 35 degree half-angle cone around a jet axis defined by the tracks and clusters.

$|d_0| \leq 2 \text{ cm}$  point of closest approach of the track to the interaction point in the  $x$ - $y$  plane.

$|z_0| \leq 75 \text{ cm}$  point of closest approach of the track to the interaction point in the  $z$ -direction.

$R_{min} \leq 75 \text{ cm}$  radius of the first jet chamber hit.

- Good cluster definition:

$N_{blk} \geq 1$  number of calorimeter blocks in the cluster.

$E_{cls} \geq 0.1 \text{ GeV}$  total energy in the cluster.

- Multihadronic events rejection cuts:

$1 \leq N_{charged}^{Total} \leq 6$  the number of good charged tracks.

$N_{chrg}^{Tot} \leq 10.$  the number of good ECAL clusters.

- Two photon events rejection cuts:

$E_{vis} \geq 0.03 E_{CM}$   $E_{vis} = \sum_{jet} Max(E_{cluster}, E_{track}); E_{CM} = 2E_{beam}.$

$\theta_{acol} \leq 15^\circ$  the angle between the 2 jet directions.

- Cosmic rays rejection cuts:

$|d_0|_{min} \leq 5 \text{ mm}$  minimum  $d_0$  of all tracks in event.

$|z_0|_{min} \leq 20 \text{ cm}$  minimum  $z_0$  of all tracks in event.

$|z_0|_{ave} \leq 20 \text{ cm}$  average  $z_0$  of all tracks in event with good  $|z_0|$ .

$|t_{meas} - t_{exp}| \leq 10 \text{ ns}$   $t_{meas}$  and  $t_{exp}$  are measured and expected times of flight.

Next, electron and muon pair events are identified and removed from the lepton pair sample.

- Electron pair events are identified by selecting events that satisfy at least one of the following:

$$\sum E_{cluster} \leq 0.8E_{CM}, \text{ or}$$

$$\sum E_{cluster} + 0.3 \sum E_{track} \leq E_{CM}.$$

- Muon pair events are identified by selecting events where both jets are identified as muons by one of three detectors (ECAL,HCAL and MUON) and where the total track and ECAL energy is more than 60% of the centre-of-mass energy. The criteria for a jet to be identified as a muon will be discussed in section 4.4.

After applying these criteria to the data sample, 83474 events remain as tau pair candidates. Monte Carlo sample give a tau-pair selection efficiency of  $54.3 \pm 0.1\%$ , which corresponds to an efficiency of approximately 93% within the barrel detector. The background contamination is estimated [20] from the Monte Carlo samples to be  $1.83 \pm 0.30\%$ . The analysis presented here is insensitive to background contamination.

### 4.3 Selection of Pions

Charged pions (and to a smaller extent charged kaons) from the process  $\tau^- \rightarrow \pi^-(K^-)\nu_\tau$  are the most useful particles to test the hadronic calorimeter because they are observable as isolated charged tracks and their momenta can be measured in the central detector. Furthermore, pions that deposit only a small amount of energy in the ECAL can be used to measure the intrinsic HCAL energy resolution. The pion samples used in this analysis were selected from the MC and data tau pair samples described above. Initially events identified as electrons or muons by the OPAL tau working group standard selection procedure [21, 22] were rejected from the sample. Fig. 4.1 shows the pion candidates

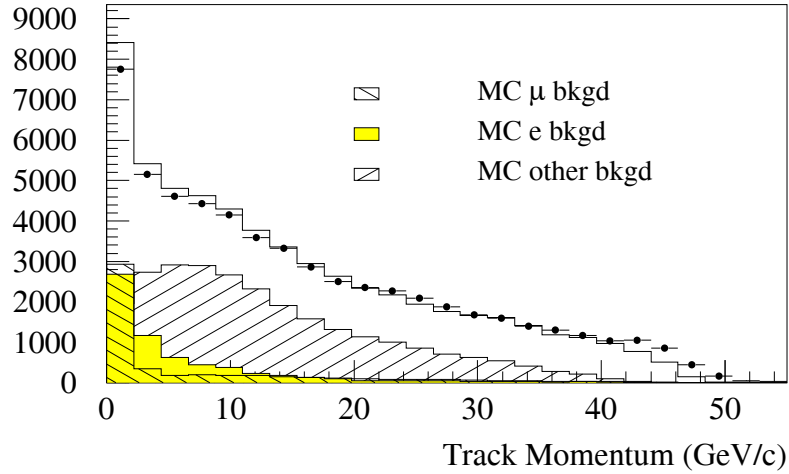


Figure 4.1: *The pion candidates momentum distribution after initial rejection for data (points) and MC (histogram).*

momentum distributions after initial selection. There is a large background of nonpions, therefore a more stringent selection is applied.

The following selection procedure is used to select a more pure sample of single charged pions.

1. Select a good event in the barrel:

$ \cos \theta  < 0.68$	average value of $ \cos \theta $ for the two jets.
$N_{chrg} = 1$	number of good charged tracks assigned to the jet.
$E_{HC} \geq 120 \text{ MeV}$	the total energy in the HCAL.

2. The following criteria reject mainly the process  $\pi^0 \rightarrow \gamma\gamma$  and some charged pions that shower early.

$M_{pres} < 4$	the presampler multiplicity in the jet.
----------------	---

$\delta\phi_{Max} < 0.5^\circ$       the difference in azimuthal angle between the track and the nearest presampler cluster.

$N_{cluster} = 1$       number of ECAL clusters in the jet.

3. A  $\tau \rightarrow \mu\nu\bar{\nu}$  candidate rejection cuts:

- The HCAL and MUON detectors are used to further reduce the background from  $\tau \rightarrow \mu\nu\bar{\nu}$  events. These two detectors have gaps in the geometric acceptance that must be taken into account.

- In the regions where neither has a gap, we *reject* candidates as being muons if

$$N_{layers}^{HC/MU} \geq 3, \text{ and } N_{hits/layer}^{HC} \leq 4$$

or

$$N_{layers}^{HC/MU} = 2, \text{ and } N_{hits/layer}^{HC} < 3,$$

where  $N_{layers}^{HC/MU}$  is the number of layers containing signal out of a possible seven (consisting of the outer three HCAL layers and all four outer MUON chamber layers), and  $N_{hits/layer}^{HC}$  is the the average number of strip hits per layer in the HCAL.

- In the region where only the MUON detector has a gap, we *reject* candidates as being muons if

$$N_{hits/layer}^{HC} \leq 4$$

- In the region where only the HCAL detector has a gap, we *reject* candidates as being muons when

$$N_{layers}^{MU} \geq 2$$

where  $N_{layers}^{MU}$  is the number of associated outer MUON chamber layers with a signal.

- To reduce muon contamination even more and to get an accurate momentum measurement, the track momentum must be:

$$5 \leq p_{trk} \leq 50 \text{ GeV}/c.$$

4. To further reject any remaining electrons and  $\rho$  background, the ratio of the ECAL cluster energy to the track momentum must satisfy:

$$E_{ec}/p_{trk} < 0.8.$$

After all the requirements have been applied to the tau pair data sample, 6057  $\tau^- \rightarrow \pi^-(K^-)\nu_\tau$  candidates remain. The same selection is applied to the Monte Carlo tau pair sample, resulting in 10591  $\tau^- \rightarrow \pi^-(K^-)\nu_\tau$  candidates with an estimated background contamination of 4%, due mostly to  $\tau^- \rightarrow \pi^-\pi^0$  and  $\tau^- \rightarrow \mu^-\bar{\nu}_\mu\nu_\tau$

A subset of the pion sample is selected by requiring

$$E_{ec} < 1.5 \text{ GeV}.$$

These events have minimal interaction in the ECAL, and thus are called *minimum EM-interacting* events. These events are useful for measuring the bare HCAL resolution. There are 2447 minimum EM-interacting pion candidates in the tau pair data sample, and 3836 minimum EM-interacting pion candidates in the Monte Carlo tau pair sample with an estimated background of 1.4%.

Fig. 4.2(a) shows the momentum distributions for data and Monte Carlo tau pair sample. Fig. 4.2(b) shows the momentum distributions after all pion cuts for data and Monte Carlo. The distributions (Figs. 4.1 and 4.2) are uniform over the full momentum range and the data and MC agree well for all distributions. The pion cuts do not introduce any significant bias in the momentum distributions of the  $\tau^- \rightarrow \pi^-\nu_\tau$  events.

## 4.4 Selection of muons

Muons and minimum EM-interacting pions behave similarly in the ECAL and presampler. Therefore the  $\tau^- \rightarrow \mu^-\bar{\nu}_\mu\nu_\tau$  candidate sample was used to estimate the behaviour expected



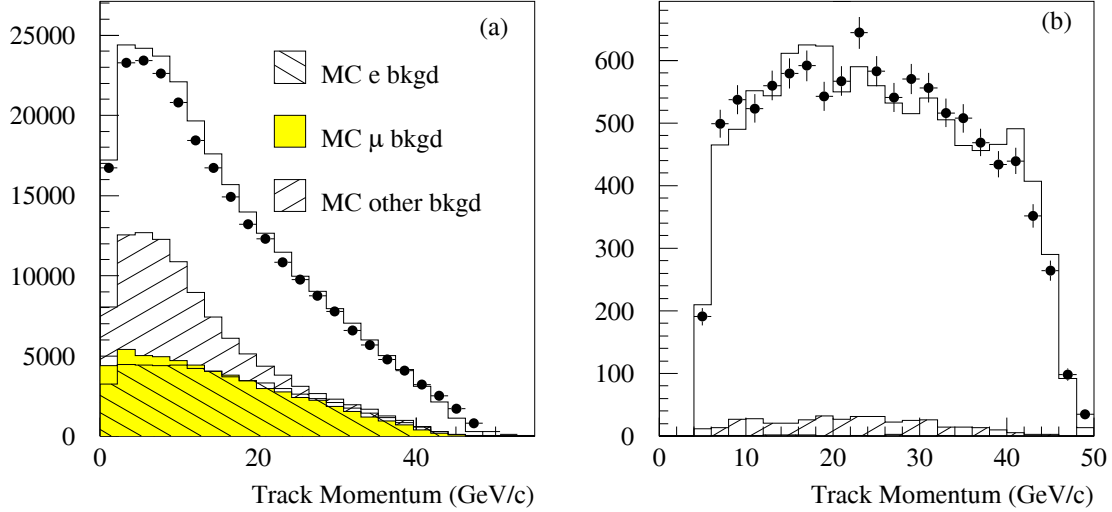


Figure 4.2: Fig.(a) shows the tau pair sample momentum distribution for data (points) and MC (histogram); Fig.(b) shows the single pion candidates momentum distribution for data (points) and MC simulation (histogram) after all cuts applied.

for the minimum EM-interacting pions. The following selection [21, 22] is used to identify muons.

1. A jet should contain exactly one good track with  $|\cos\theta| < 0.68$ .
2. A  $\tau^- \rightarrow \mu\bar{\nu}\nu$  candidate must satisfy at least *two* of the following three requirements:
  - Identification by MUON chamber:  $N_{layers}^{MU} \geq 2$   
where  $N_{layers}^{MU}$  is the number of layers with signals in MUON chamber.
  - Identification by HCAL:  $N_{layers}^{HC} \geq 4$  and  $N_{hits/layers}^{HC} < 3$   
where  $N_{layers}^{HC}$  is the number of HCAL layers containing signals;  $N_{hits/layer}^{HC}$  is the the average number of strip hits per layer in the HCAL.
  - Identification by ECAL:  $E_{ec} < 2 GeV$   
where  $E_{ec}$  is ECAL energy.

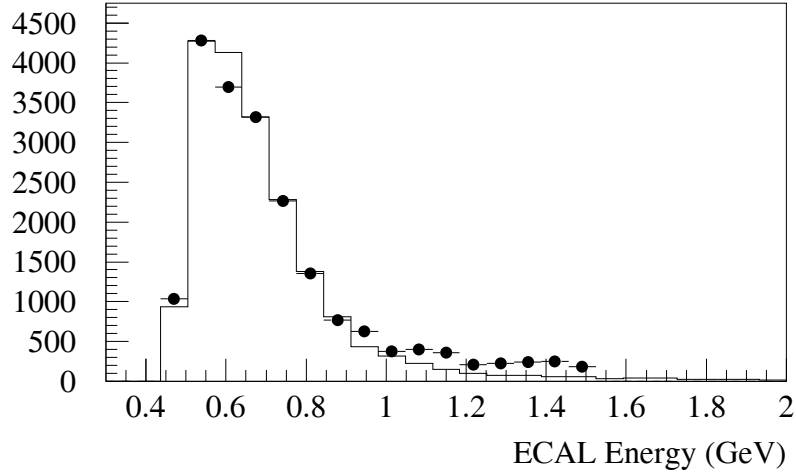


Figure 4.3: *The ECAL energy distributions for muons (line) and minimum EM-interacting pions (points).*

- comparison with minimum EM-interacting pions under the same momenta conditions:

$$5 \leq p_{trk} \leq 50 \text{ GeV}/c$$

After all requirements, 19184  $\tau \rightarrow \mu\nu\bar{\nu}$  candidates are selected from the 1991 to 1994 data samples, and 38073 Monte Carlo muon events are selected. Fig. 4.3 shows the ECAL energy distributions for the selected muon and minimum EM-interacting pion events. The behaviour of minimum EM-interacting pions in the ECAL is similar to that of muons as expected.

## 4.5 Pion Shower Profile

In section 3.2.1 the general properties of hadronic showers were discussed. In this section, we use the minimum EM-interacting pion samples described earlier to get a qualitative understanding of the longitudinal profile of the hadron showers. The energy of the hadronic shower was determined by summing the energy from each tower within the jet. The longitudinal profile mapping was obtained by summing over the number of hits in

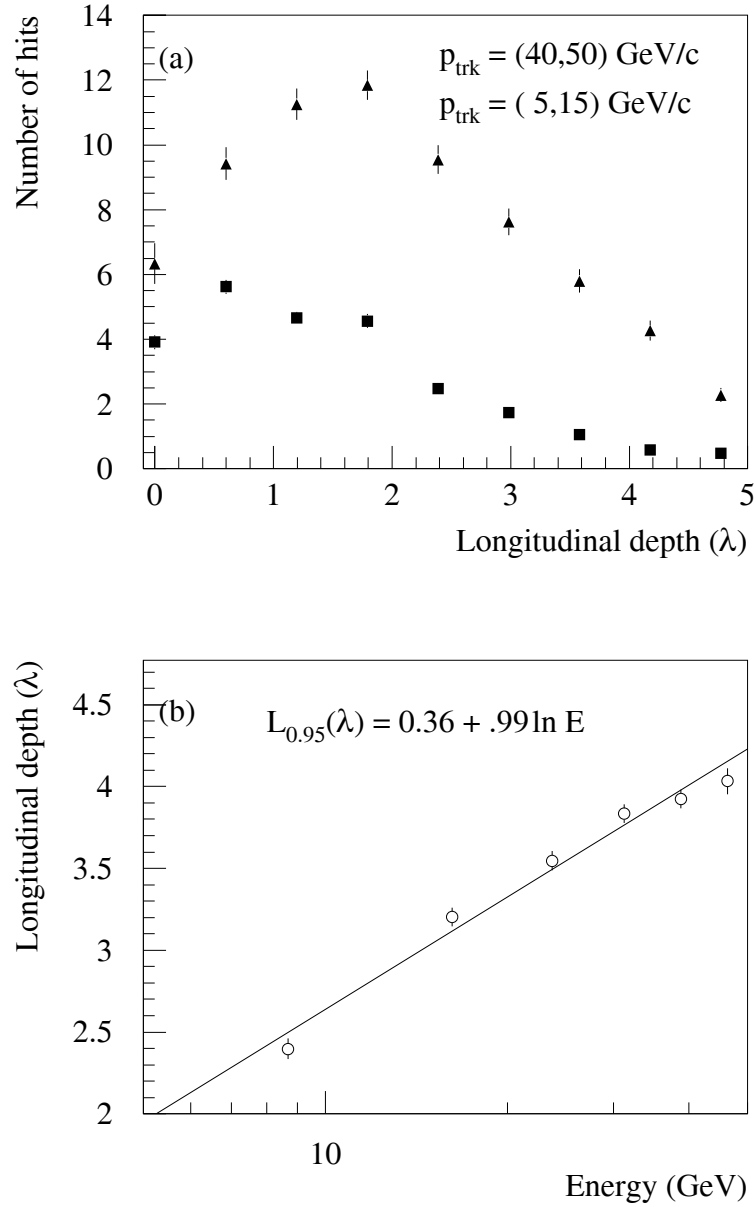


Figure 4.4: (a) Longitudinal hadronic shower development induced by pions in two different momentum bins. (b) The shower depth for 95% energy containment as a function of incident energy.

each layer, provided by the strip signals within the jet. Longitudinal energy deposition profiles are characterized by a sudden onset at the first interaction point followed by a more gradual development with a maximum at a depth [7]

$$x/\lambda \equiv t_{max} \approx 0.2 \ln(E) + 0.7, \quad (4.1)$$

where  $E$  is the energy in the shower. Fig. 4.4(a) shows the longitudinal hadronic shower development in two different energy bins for minimum EM-interacting pion data. It shows the expected features.

Fig. 4.4(b) shows the hadronic shower depth for 95% energy containment as a function of incident energy. The longitudinal depth with 95% energy containment is measured from the face of the HCAL to the layer in which the running sum reached 95% of the total shower hits. The dependence of  $\theta$  on the amount of iron traversed has been taken into account. For very energetic particles in the HCAL the longitudinal depth measurement is not accurate because the HCAL in OPAL is only 4.77 interaction lengths. It can be shown [7] that for particles around 50 GeV, approximately 6 interaction lengths are required for 95% energy containment. Nevertheless, the expected logarithmic dependence of the shower depth with particle energy is observed.

# Chapter 5

## Intrinsic Energy Resolution

After discussing the hadronic shower in detail in chapter 3 and the pion selection in chapter 4, we now return to the aim of this thesis: studying the response of the calorimeter to hadrons, calibrating the HCAL energy against the measured momentum of the pion and measuring the intrinsic energy resolution of the hadron calorimeter.

### 5.1 Energy Calibration and Corrections

The energy measured in the HCAL,  $E_{HC}$ , can be written in terms of the initial particle energy,  $E_i$ , and the energy deposited in the ECAL,  $E_{EC}$ , as

$$E_i = E_{HC} + E_{EC}. \quad (5.1)$$

In this section we are only considering minimum EM-interacting pions, and so the energy deposited in the ECAL can be calculated from the Bethe-Bloch formula (see Fig. 5.1). The average ionizing energy loss,  $\Delta E_{mi}$ , is calculated to be 0.392  $GeV$  for incident particle energies from 10 - 45  $GeV$ . The incident pion energy,  $E_i$ , can be obtained by the relation between the energy and momentum of a particle,

$$\frac{E_\pi^2}{c^2} = p_\pi^2 + m_\pi^2 c^2. \quad (5.2)$$

where  $m_\pi = 0.14 GeV/c^2$ . For convenience, we set  $c \equiv 1$ . The mass of the pion will be ignored, since it is very small compared with the momentum of the incident pion

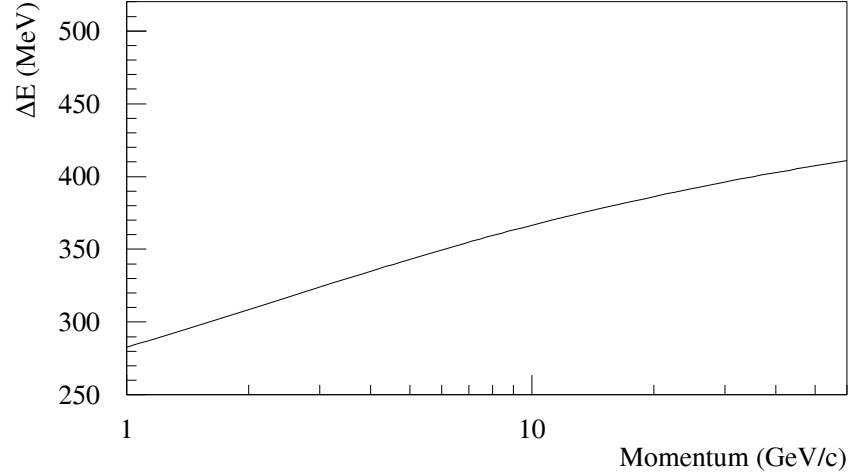


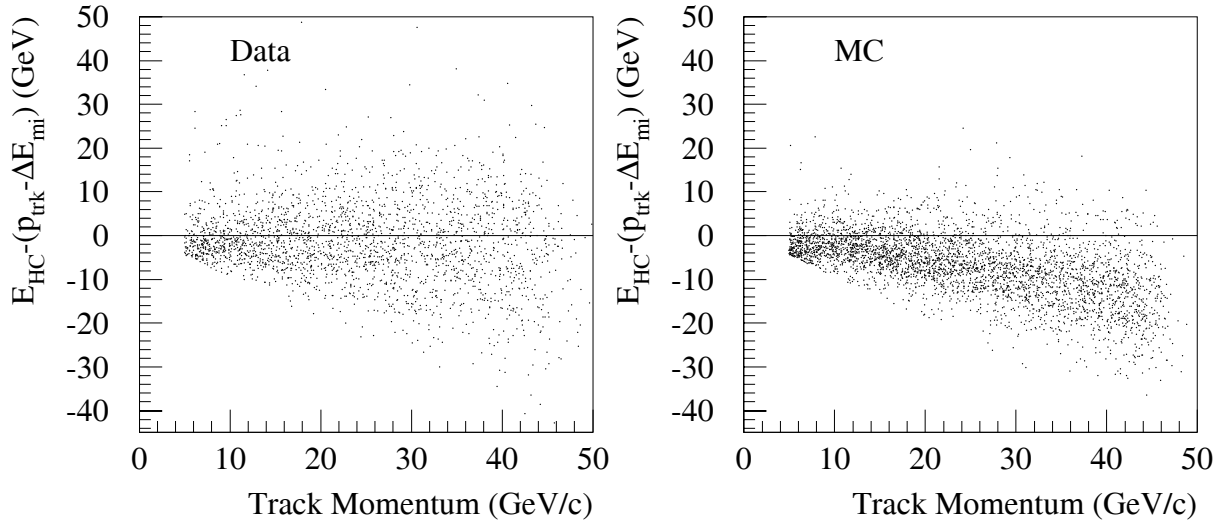
Figure 5.1: The plot shows the energy loss by ionization,  $\Delta E$ , in ECAL.

(5 – 50 GeV). Thus the incident pion energy equals the momentum of the pion,  $p_\pi$ .

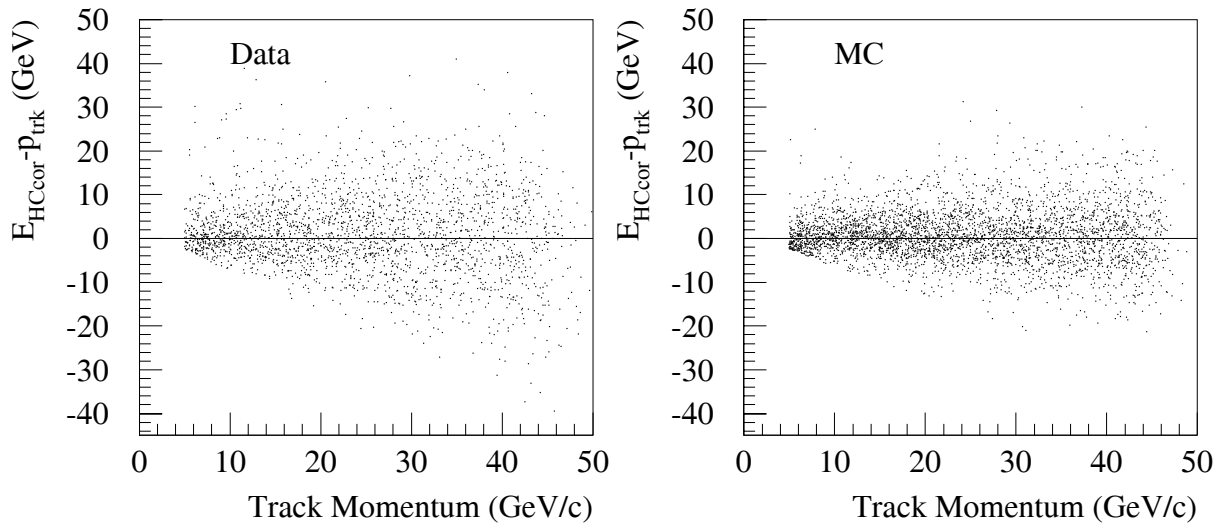
The momentum spectrum of the minimum EM-interacting pions has been divided into six bins of 7.5 GeV each (5-12.5, 12.5-20, 20-27.5, 27.5-35, 35-42.5, 42.5-50 GeV), corresponding to six ‘proper’ incident energies (8.67, 16.22, 23.73, 31.24, 38.74, 46.24 GeV. See appendix A).

For particles which stop in the HCAL, the energy deposited in the HCAL should be equal to the incident energy of the particle at the HCAL. This energy can be approximated by  $(p_{trk} - \Delta E_{mi})$  for minimum EM-interacting events, where  $p_{trk}$  is the measured track momentum. Thus, the difference  $E_{HC} - (p_{trk} - \Delta E_{mi})$  should be approximately zero for minimum EM-interacting events. Fig. 5.2(a) shows the difference  $E_{HC} - (p_{trk} - \Delta E_{mi})$  versus the initial pion momenta for data and Monte Carlo events. The plots show that the difference is not zero, especially for Monte Carlo events. Thus the HCAL energy calibration must be corrected.

The mean value of  $E_{HC} - (p_{trk} - \Delta E_{mi})$  is determined in each momentum bin for



(a) Before correction of HCAL energy



(b) After correction of HCAL energy

Figure 5.2: The difference between the measured and expected HCAL energy versus the incident energy.

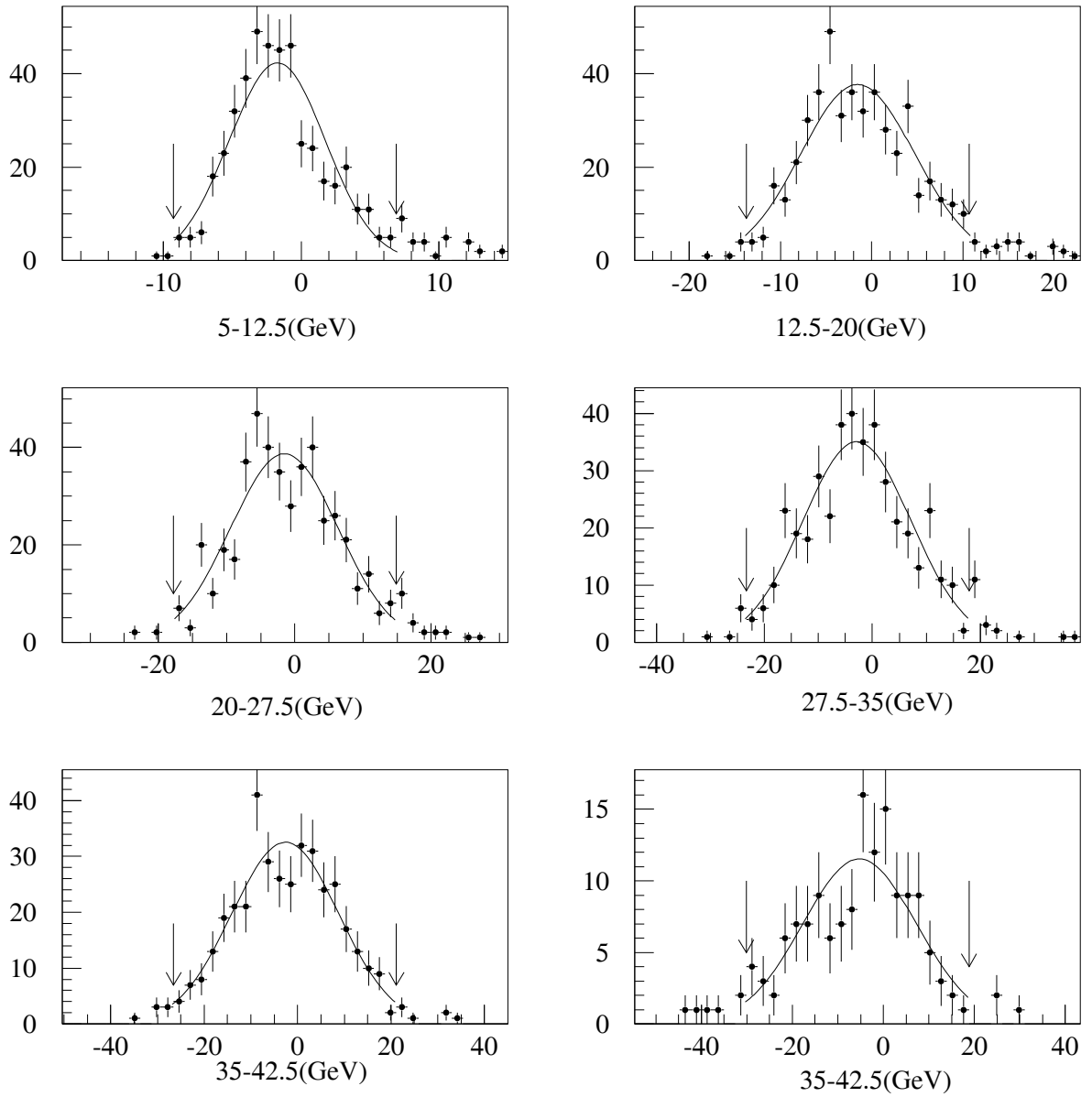


Figure 5.3:  $E_{HC} - (p_{trk} - \Delta E_{mi})$  spectrum for six momentum bins. The dot with error bar represents the data, and the curved lines are the results of the fit over a range of  $\pm 2\sigma$ .



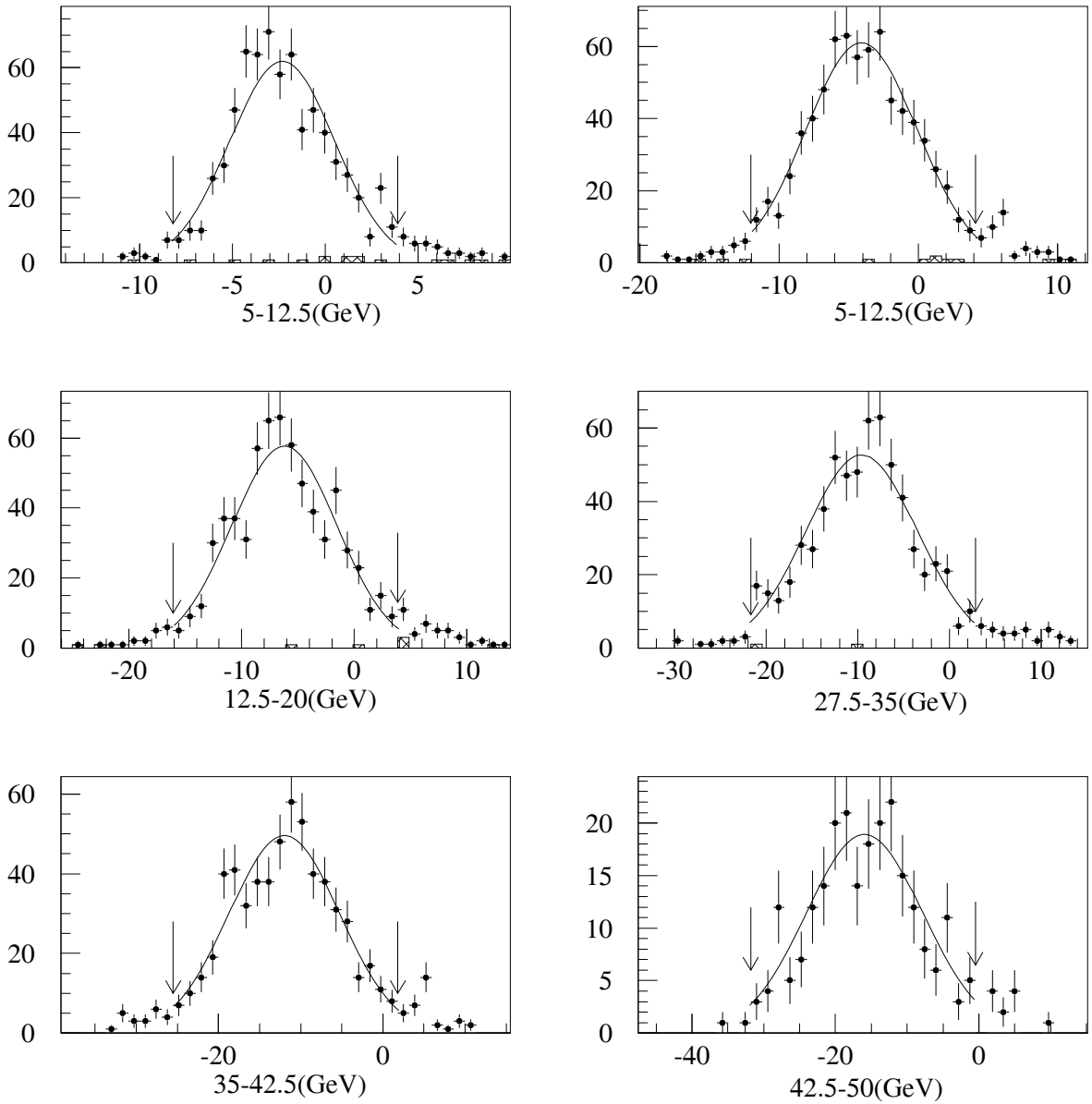


Figure 5.4:  $E_{HC} - (p_{trk} - \Delta E_{mi})$  spectrum for six momentum bins. The dot with error bar represents the Monte Carlo simulated data, and the curved lines are the results of the fit over a range of  $\pm 2\sigma$ . The hatched histogram represents the background in the Monte Carlo.

DATA				
$E(\text{GeV})$	$\mu$	$\sigma$	$\chi^2/\nu$	bin size
8.67	$-1.73 \pm 0.18$	$3.49 \pm 0.15$	32.01/17	0.81
16.22	$-1.53 \pm 0.34$	$6.25 \pm 0.33$	26.08/17	1.22
23.73	$-1.55 \pm 0.42$	$7.87 \pm 0.39$	35.88/17	1.63
31.24	$-2.86 \pm 0.55$	$10.00 \pm 0.52$	24.14/17	2.06
38.74	$-2.64 \pm 0.66$	$11.44 \pm 0.62$	14.03/17	2.38
46.24	$-5.24 \pm 1.19$	$12.48 \pm 1.19$	15.13/17	2.45
MC				
$E(\text{GeV})$	$\mu$	$\sigma$	$\chi^2/\nu$	bin size
8.67	$-2.32 \pm 0.12$	$2.82 \pm 0.11$	41.22/17	0.61
16.22	$-4.08 \pm 0.17$	$3.99 \pm 0.16$	9.59/17	0.81
23.73	$-6.21 \pm 0.20$	$4.67 \pm 0.19$	30.30/17	1.00
31.24	$-9.96 \pm 0.28$	$6.10 \pm 0.26$	27.97/17	1.23
38.74	$-12.36 \pm 0.31$	$6.75 \pm 0.30$	16.89/17	1.37
46.24	$-16.31 \pm 0.63$	$8.17 \pm 0.63$	16.72/17	1.57

Table 5.1: Fitting parameters of  $E_{HC} - (p_{trk} - \Delta E_{mi})$  for data and MC.

data and Monte Carlo events by a log-likelihood fit to a Gaussian function. The results are shown in Figs. 5.3 and 5.4. In Fig. 5.4 there is high percentage of non-pion background in the right side tail. Therefore the Gaussian log-likelihood fit was done iteratively over a range of  $\pm 2\sigma$  with the number of bins in each fit fixed to 20. Table 5.1 shows the results of the fits. Fig. 5.5 shows the six mean values of the Gaussian fits plotted as a function of momentum for data and Monte Carlo events. The open circles in this figure represent the data, and the straight line is a fit of the mean values of  $E_{HC} - (p_{trk} - \Delta E_{mi})$  to a linear function,

$$E_{HC} - (p_{trk} - \Delta E_{mi}) = ap_{trk} + b. \quad (5.3)$$

The corrected HCAL energy,  $E_{HC\text{cor}}$ , should equal  $(p_{trk} - \Delta E_{mi})$  on average. Therefore  $E_{HC\text{cor}}$  can be written as

$$E_{HC\text{cor}} = E_{HC} - (ap_{trk} + b). \quad (5.4)$$

where  $E_{HC}$  is measured HCAL tower energy. In Fig. 5.5 the stars represent the Monte

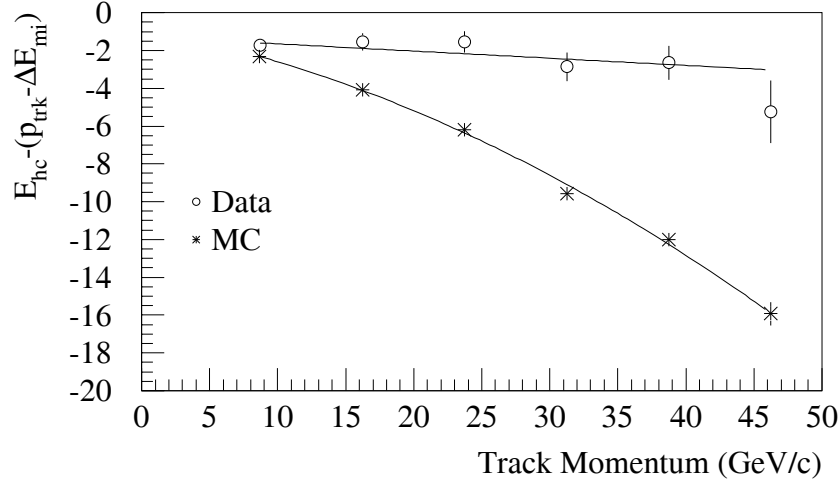


Figure 5.5: The mean values of  $E_{HC} - (p_{trk} - \Delta E_{mi})$  for six momentum bins for pion data and Monte Carlo events before correction and the results of the fits described in the text. The  $\chi^2/\nu = 7.84/4$  for data and  $\chi^2/\nu = 4.56/3$  for Monte Carlo events.

Carlo simulated data, and the curved line is a fit of the mean values of  $E_{HC} - (p_{trk} - \Delta E_{mi})$  to a quadratic function

$$E_{HC} - (p_{trk} - \Delta E_{mi}) = ap_{trk}^2 + bp_{trk} + c. \quad (5.5)$$

The corrected energies for MC events are given by the expression

$$E_{HC\,cor} = E_{HC} - (ap_{trk}^2 + bp_{trk} + c). \quad (5.6)$$

The values of the parameters determined from the fits for data and MC are listed in

DATA	a	$-0.038 \pm 0.015$
	b	$-1.269 \pm 0.260$
MC	a	$-0.004 \pm 0.001$
	b	$-0.137 \pm 0.035$
	c	$-0.808 \pm 0.328$

Table 5.2: Polynomial correction parameters of HCAL energy for data and MC.

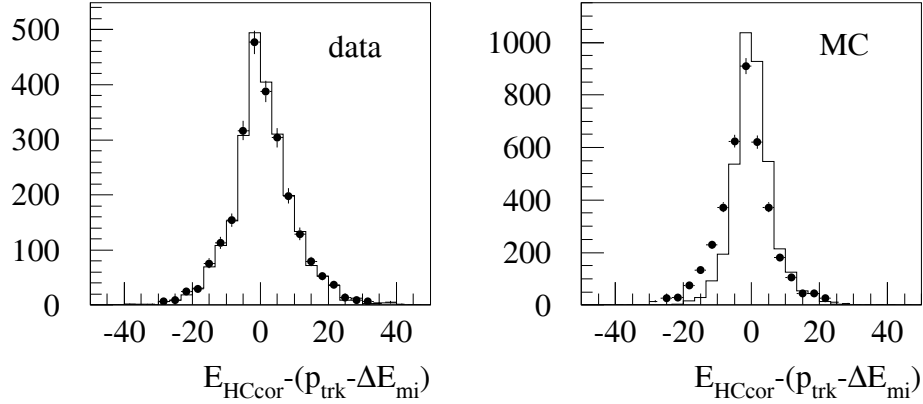


Figure 5.6: This figure shows the distributions of  $E_{HCcor} - (p_{trk} - \Delta E_{mi})$  using the track momentum (histogram) and the measured HCAL energy (dots) in the correction function. The two methods of determining the corrected energy are equivalent for data and MC.

table 5.2. These are used to correct the measured HCAL tower energies.

Fig. 5.2(b) shows the difference  $E_{HCcor} - (p_{trk} - \Delta E_{mi})$  versus the initial pion momenta for data and Monte Carlo events. They are now distributed around zero.

For neutral hadrons (eg. neutrons) the track momentum is unknown. However, the measured HCAL energy can be used in place of the initial track momentum to calculate the corrected HCAL energy. Fig. 5.6 shows the distributions of  $E_{HCcor} - (p_{trk} - \Delta E_{mi})$  using the track momentum and the measured HCAL energy in the correction function. These distributions are equivalent for both the data and the Monte Carlo.

## 5.2 The HCAL Energy Resolution

The energy resolution of a calorimeter is given by the ratio,  $\sigma/E$ , where  $\sigma$  is the width of the energy distribution for particles with incident energy  $E$ . Since we are using finite width momentum bins, we must take the difference between the measured and incident energies,  $E_{HC} - (p_{trk} - \Delta E_{mi})$ , to produce a Gaussian distribution, from which we can

measure  $\sigma$ . We could equivalently use the corrected HCAL energy,  $E_{HC\text{cor}}$ , instead of  $E_{HC}$ . The widths of the distributions using either energy are consistent within statistical uncertainties, since the energy correction is linear for the data and approximately linear for the Monte Carlo.

For this analysis, we used the uncorrected HCAL energy in order to reduce the extra uncertainties introduced by the fitted coefficients of the correction functions. The widths,  $\sigma_{(E_{HC}-p_{trk})}$ , in each momentum bin are given in table 5.1. The momentum resolution will, in general, also contribute to the width of the distributions. The total width can be written as

$$\sigma_{(E_{HC}-p_{trk})}^2 = \sigma_{E_{HC}}^2 + \sigma_{p_{trk}}^2. \quad (5.7)$$

However,  $\sigma_{E_{HC}}$  is the dominant term and so we assume

$$\sigma_{(E_{HC}-p_{trk})} \simeq \sigma_{HC}. \quad (5.8)$$

The resolution can be determined by fitting the model discussed in chapter 3 to the measured widths. The HCAL energy resolution fitted with  $\sigma/E = a/\sqrt{E}$  (*i.e.* only sampling and shower fluctuations included in the fit) is shown in Fig. 5.7(a). This figure shows that this is not a good representation of the HCAL energy resolution.

The HCAL energy resolution in the data, determined from  $\sigma/E = a + b/\sqrt{E}$  (*i.e.* also includes detector response imperfections), is:

$$\frac{\sigma_{HC}}{E} = (20.1 \pm 2.6)\% + \frac{(62.8 \pm 11.5)\%}{\sqrt{E}}. \quad (5.9)$$

This is shown in Fig. 5.7(b). The result from the Monte Carlo sample was calculated to be

$$\frac{\sigma_{HC}}{E} = (4.4 \pm 1.5)\% + \frac{(80.9 \pm 7.1)\%}{\sqrt{E}}. \quad (5.10)$$

This is also shown in Fig. 5.7(b). We can see from the plot and  $\chi^2$  that the two parameter function gives a much better fit than the one parameter fit.

The apparently low value of the data point in the lowest momentum bin induces a large constant term and reduces the energy dependent term. The systematic error for the energy

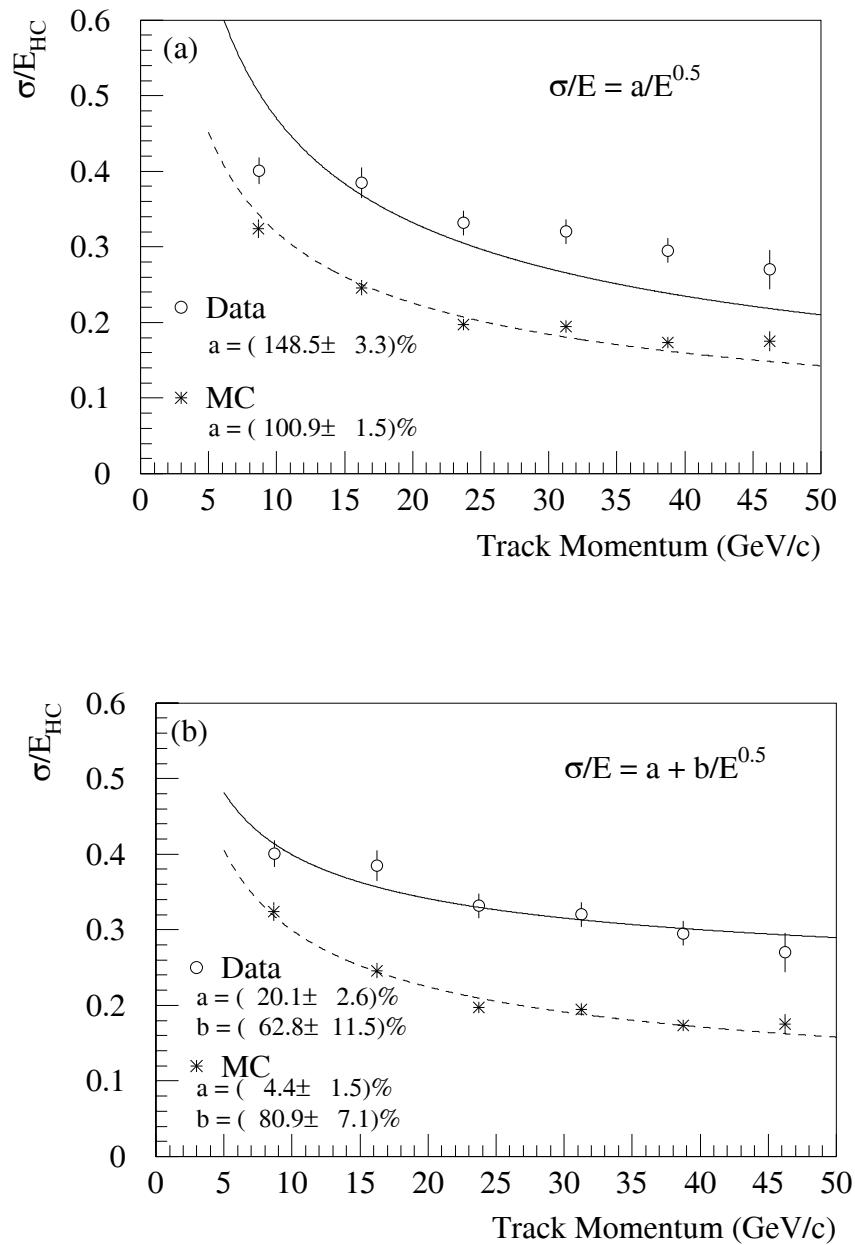


Figure 5.7: (a) The HCAL energy resolution fitted with one parameter with a  $\chi^2$  value per degree of freedom of  $\chi^2/\nu = 64.75/5$  (data),  $\chi^2/\nu = 13.00/5$  (MC); (b) The HCAL energy resolution fitted with two parameters with a  $\chi^2$  value per degree of freedom of  $\chi^2/\nu = 3.62/4$  (data) and  $\chi^2/\nu = 4.46/4$  (MC).

resolution arising from neglecting the momentum resolution as given by equation (2.1) is 0.04 when the momentum is  $25 \text{ GeV}$ .

# Chapter 6

## Combined Energy Resolution

In the previous section the HCAL energy resolution was measured by using minimum EM-interacting pions. However most hadrons begin to shower in front of the HCAL, so the hadronic energy resolution for the combined electromagnetic and hadron calorimeter is more useful.

### 6.1 ECAL Energy weighting

The combined calorimeter can be considered as a single hadron calorimeter for incident hadrons. However, the lead glass in ECAL is sensitive only to the Čerenkov light generated by fast moving charged particles. It is therefore insensitive to the slow moving nucleon fragments in hadronic showers, and thus the lead glass response to some hadrons will be different than the response to the fast-moving lighter charged particles at the same energy. Consequently an energy weighting for the ECAL is required. The total hadronic energy in the calorimeters can be expressed as:

$$E_h = \alpha E_{EC} + E_{HC_{cor}} \quad (6.1)$$

where  $\alpha$  is an energy weighting factor for the ECAL,  $E_{EC}$  is the electron calibrated ECAL energy, and  $E_{HC_{cor}}$  is the corrected HCAL energy. Again we assume the incident pion energies equal the momenta of the pions.



The ECAL energy weighting factor,  $\alpha$ , is determined by minimizing the sum over all events of the square of the difference between the incident energy,  $E_i = p_{trk}$ , and the measured energy,  $\alpha E_{EC} + E_{HCcor}$ . This can be written as

$$\chi^2 = \sum_1^N \frac{[p_{trk} - (\alpha E_{EC} + E_{HCcor})]^2}{\sigma^2}, \quad (6.2)$$

where  $\sigma$  is uncertainty for the combined calorimeter for each event. Two expressions of  $\sigma$  have been examined. The first one is:

$$\sigma = \sqrt{\alpha E_{EC} + E_{HCcor}}, \quad (6.3)$$

which makes use of the underlying Poisson statistics of the shower. The second expression is the calculated resolution of section 5.2,

$$\sigma = \sigma_{HC}(p_{trk}) = ap_{trk} + b\sqrt{p_{trk}}, \quad (6.4)$$

where the parameters  $a$  and  $b$  for both data and MC events are given in formulae 5.9 and 5.10. Here it is assumed the combined calorimeter can be seen as a single hadron calorimeter when the incident particles are hadrons with a resolution approximately the same as the HCAL. The minimization is performed in each of the six momentum bins. Fig. 6.1 shows the signed  $\chi$  distributions (with  $\alpha = 1$ ) given by

$$\chi_a = \frac{p_{trk} - (E_{EC} + E_{HCcor})}{E_{EC} + E_{HCcor}} \quad (6.5)$$

and

$$\chi_b = \frac{p_{trk} - (E_{EC} + E_{HCcor})}{(ap_{trk} + b\sqrt{p_{trk}})^2}. \quad (6.6)$$

The  $\chi$  distribution is symmetric in the first case but not in the second case. The long tails in these distributions give a large total  $\chi^2$ . We do not want to bias the fit by using the data in the tails. Therefore the first method (equation 6.3) of calculation of the error is used and the fit is performed using data satisfying  $-5 < \chi < 5$ . The ECAL energy weighting factors for each momentum bin are shown in table 6.1. The uncertainties obtained from

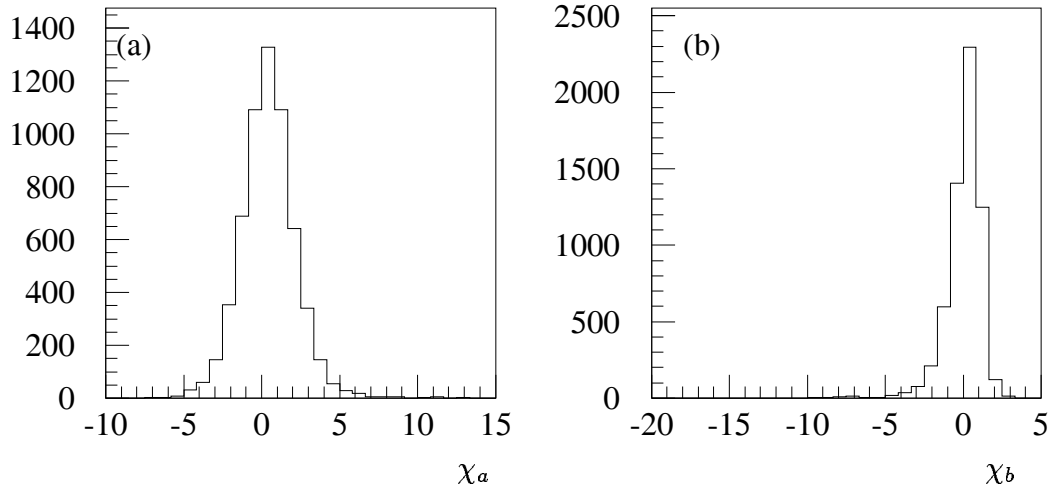


Figure 6.1: (a) The  $\chi$  distribution for formula 6.5; (b) The  $\chi$  distribution for formula 6.6.

these fits must be adjusted to reflect the large of  $\chi^2/\nu$ , where  $\nu$  is the number of degrees of freedom in each fit. We do this by scaling all values of  $\sigma$  in the denominator of  $\chi^2$  by  $\sqrt{\chi^2/\nu}$  and refitting. The resulting uncertainties are shown in table 6.1 as  $\delta\alpha_{cor}$ . The relationship between  $\alpha$  and the incident momentum for data and MC is modeled with a quadratic function as shown in Fig. 6.2 and table 6.2.

	DATA			MC		
	$\alpha$	$\chi^2/\nu$	$\delta\alpha_{cor}$	$\alpha$	$\chi^2/\nu$	$\delta\alpha_{cor}$
1	$1.56 \pm 0.04$	1.75	0.05	$1.41 \pm 0.03$	0.97	0.03
2	$1.49 \pm 0.02$	1.96	0.03	$1.20 \pm 0.02$	1.15	0.02
3	$1.35 \pm 0.02$	2.32	0.03	$1.05 \pm 0.01$	1.20	0.02
4	$1.33 \pm 0.02$	2.65	0.03	$0.94 \pm 0.01$	1.23	0.01
5	$1.40 \pm 0.02$	2.65	0.03	$0.88 \pm 0.01$	1.29	0.02
6	$1.36 \pm 0.03$	2.65	0.05	$0.84 \pm 0.02$	1.35	0.02

Table 6.1: The  $\alpha$  for six momentum bins

	DATA $\chi^2/\nu = 1.83$	MC $\chi^2/\nu = 0.21$
a	$1.749 \pm 0.086$	$1.674 \pm 0.045$
b	$-0.024 \pm 0.007$	$-0.035 \pm 0.003$
c	$0.0004 \pm 0.0001$	$0.0004 \pm 0.0001$

Table 6.2: Polynomial parameters of the  $\alpha$  as a function of the momentum for data and MC.

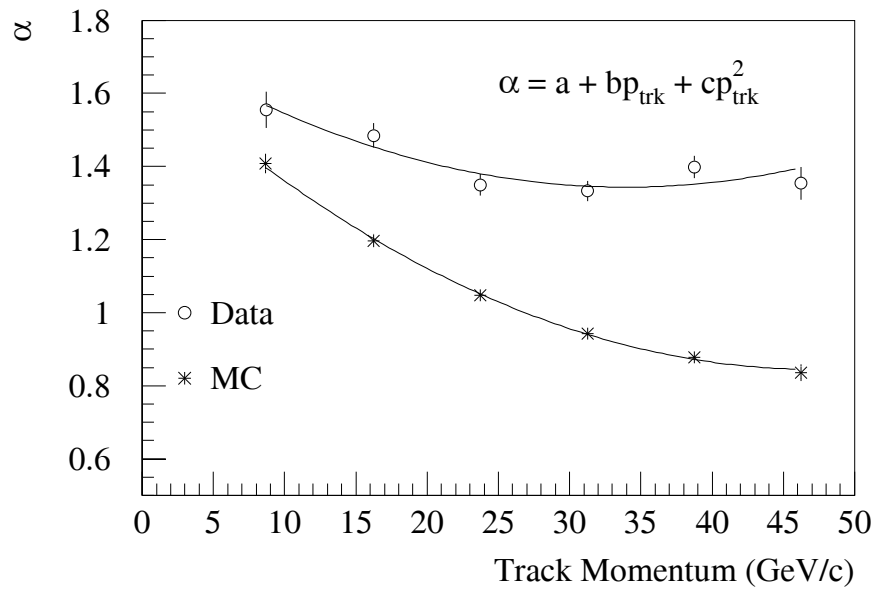


Figure 6.2: The ECAL weight,  $\alpha$ , as a function of incident momentum,  $\chi^2/\nu = 7.32/3$  for data and  $\chi^2/\nu = 0.84/3$  for MC

## 6.2 The Hadronic Energy Resolution with the Combined Calorimeter

The hadronic energy resolution with the combined calorimeter can be obtained in the same manner as described in chapter 5 but using the normalized variable  $(\alpha E_{EC} + E_{HC\text{cor}} - p_{trk})$  in the distributions. The distributions for each momentum bin for data and Monte Carlo are shown in Figs. 6.3 and 6.4. The figures show that the means of  $(\alpha E_{EC} + E_{HC\text{cor}} - p_{trk})$  are approximately zero. The means,  $\mu$ , and widths,  $\sigma$ , of each peak were determined by a Gaussian log-likelihood fit over a range of  $\pm 2\sigma$ . Twenty bins were used in each histogram for each momentum bin. The fit results are shown in table 6.3. Note that the  $\sigma$  in each momentum bin is smaller than the bare HCAL one. Thus, the total calorimeter has a better resolution than the bare HCAL.

The same procedure is applied to the quantity  $(\alpha E_{EC} + E_{HC} - p_{trk})$ , where the uncorrected HCAL energy is used. The results are consistent with the  $\sigma$ 's for  $(\alpha E_{EC} + E_{HC\text{cor}} - p_{trk})$  within the uncertainty for the same momentum bin. This is expected because the HCAL calibration correction is approximately linear. The following relation is assumed:

$$\sigma_{(\alpha E_{EC} + E_{HC\text{cor}} - p_{trk})} \simeq \sigma_{(\alpha E_{EC} + E_{HC} - p_{trk})} \simeq \sigma_{(\alpha E_{EC} + E_{HC})}, \quad (6.7)$$

where the  $\sigma_{p_{trk}}$  is ignored because it is small compared with  $\sigma_{(\alpha E_{EC} + E_{HC})}$ .

The combined energy resolution for the data, determined by fitting  $\sigma/E = a + b/\sqrt{E}$ , is

$$\frac{\sigma_{(HC+EC)}}{E} = (15.9 \pm 1.5)\% + \frac{(59.9 \pm 6.7)\%}{\sqrt{E}}, \quad (6.8)$$

and is shown in Fig. 6.5. The theoretical combined hadronic energy resolution is obtained by performing the same process on Monte Carlo events. It is

$$\frac{\sigma_{(HC+EC)}}{E} = (7.1 \pm 0.7)\% + \frac{(54.9 \pm 3.5)\%}{\sqrt{E}}, \quad (6.9)$$

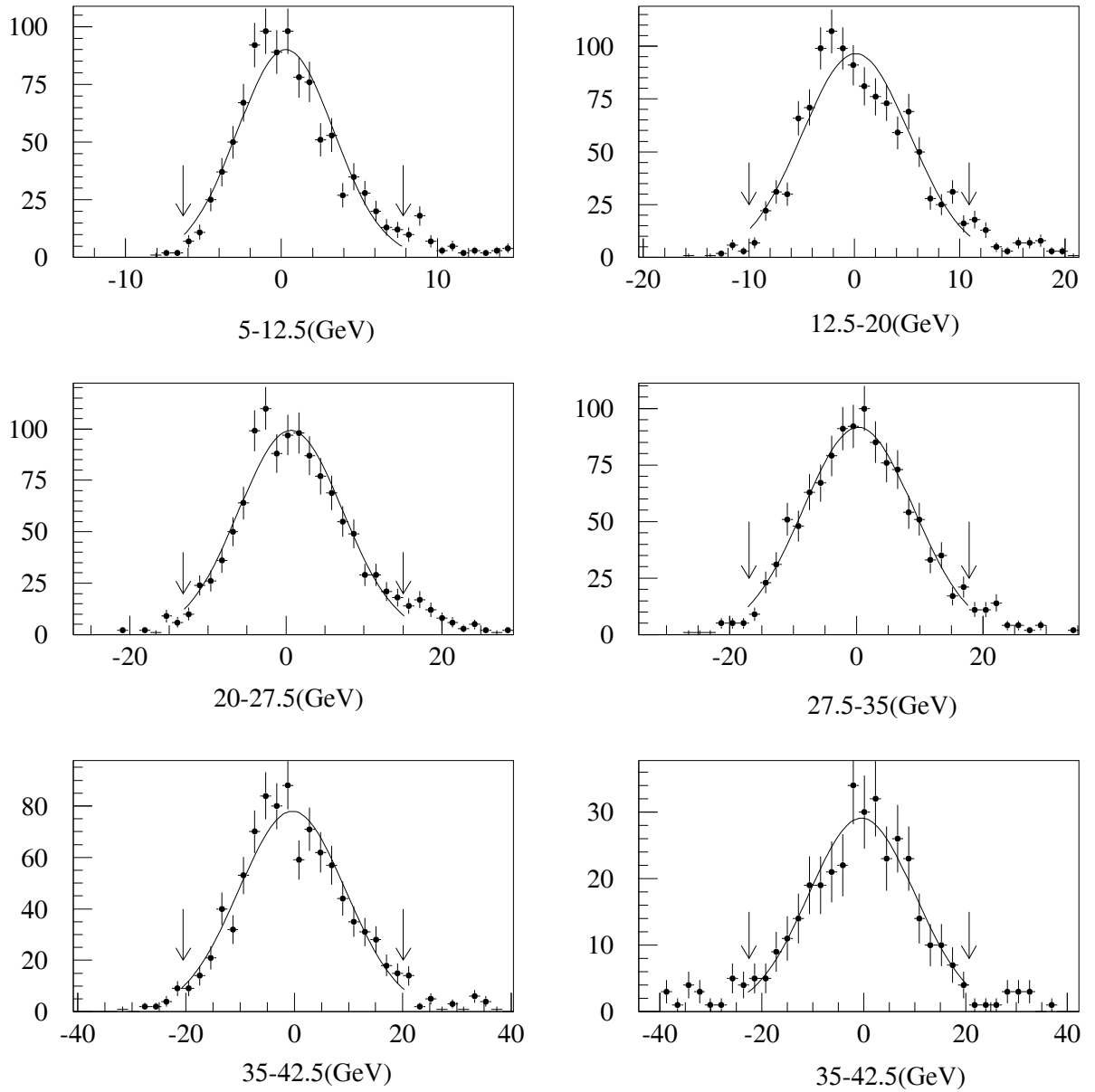


Figure 6.3:  $\alpha E_{EC} + E_{HC\text{cor}} - p$  spectrum for six momentum bins. The dot with error bar represents the data, and the curved lines are the results of the fit over a range of  $\pm 2\sigma$ .

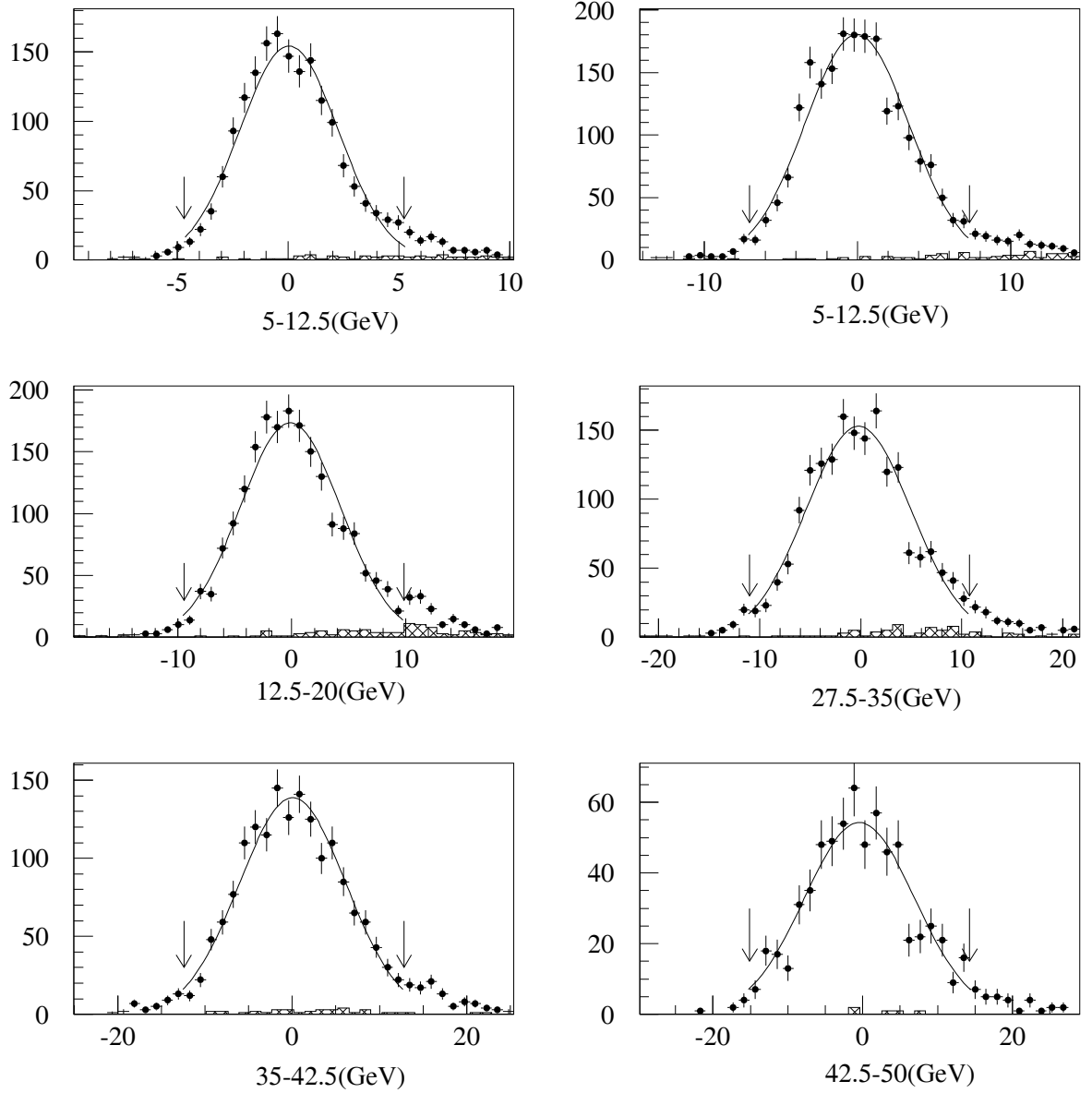


Figure 6.4:  $\alpha E_{EC} + E_{HC_{cor}} - p_{trk}$  spectrum for six momentum bins. The dot with error bar represents the Monte Carlo simulation, and the curved lines are the results of the fit over a range of  $\pm 2\sigma$ . The hatched histogram represents the background in the Monte Carlo.

DATA				
$E(\text{GeV})$	$\mu$	$\sigma$	$\chi^2/\nu$	bin size
8.67	$0.27 \pm 0.11$	$3.09 \pm 0.09$	38.59/17	0.71
16.22	$0.19 \pm 0.17$	$5.14 \pm 0.16$	42.16/17	1.04
23.73	$0.64 \pm 0.22$	$6.67 \pm 0.20$	18.36/17	1.41
31.24	$0.33 \pm 0.30$	$8.75 \pm 0.29$	14.28/17	1.74
38.74	$-0.39 \pm 0.37$	$9.86 \pm 0.35$	22.44/17	2.03
46.24	$-0.36 \pm 0.63$	$10.41 \pm 0.59$	6.46/17	2.16
MC				
$E(\text{GeV})$	$\mu$	$\sigma$	$\chi^2/\nu$	bin size
8.67	$0.04 \pm 0.06$	$2.22 \pm 0.05$	36.38/17	0.50
16.22	$-0.04 \pm 0.08$	$3.38 \pm 0.08$	43.01/17	0.72
23.73	$-0.12 \pm 0.11$	$4.41 \pm 0.10$	39.10/17	0.97
31.24	$-0.22 \pm 0.14$	$5.18 \pm 0.13$	49.64/17	1.09
38.74	$0.05 \pm 0.17$	$6.07 \pm 0.16$	23.63/17	1.26
46.24	$-0.44 \pm 0.33$	$7.34 \pm 0.32$	33.49/17	1.47

Table 6.3: Fitting parameters of  $\alpha E_{EC} + E_{HCcor} - p_{trk}$  for data and MC.

and is shown in Fig.6.5 as well. The Monte Carlo result still underestimates the measured resolution of the actual calorimeter. Again the systematic error for the energy resolution arising from neglecting the momentum resolution as given by equation (2.1) is 0.04 when momentum is 25 GeV.

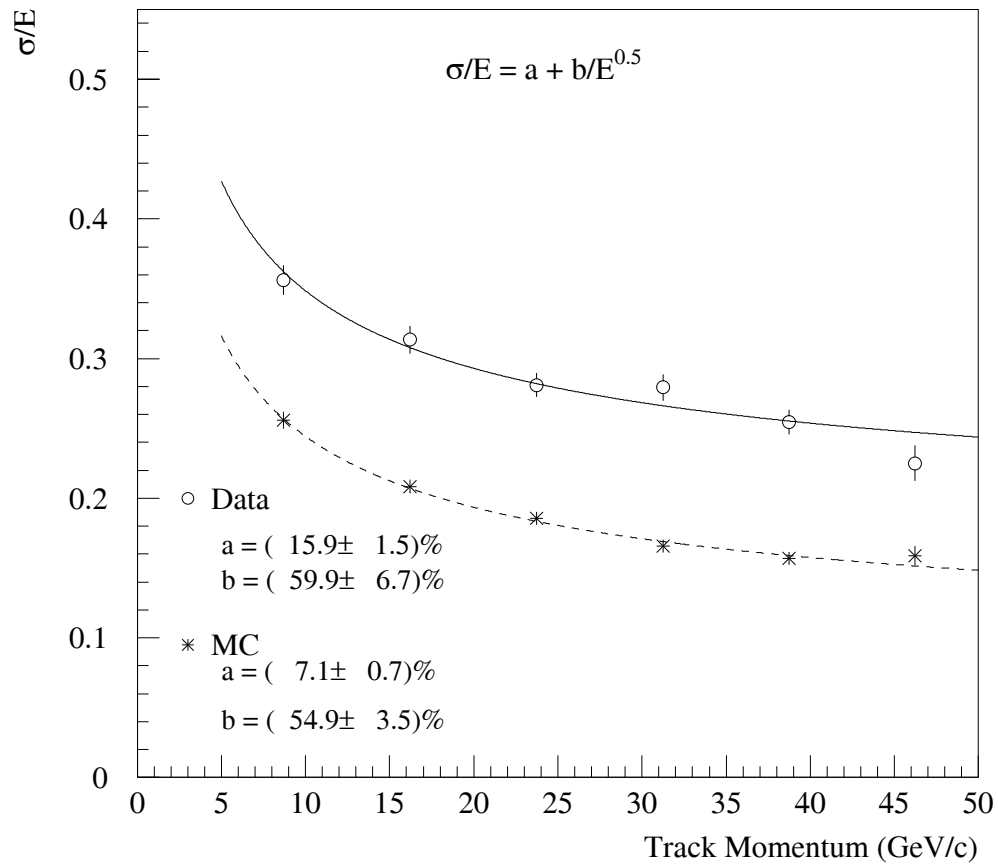


Figure 6.5: The combined energy resolution of the ECAL and HCAL to pions with a  $\chi^2$  value per degree of freedom of  $\chi^2/\nu = 6.24/4$  for data and  $\chi^2/\nu = 2.44/4$  for MC



# Chapter 7

## Conclusions and Discussion

The OPAL calorimeter response has been studied by using a selected sample of pions. The sample is over 98% pure and momentum analyzed. We have seen that pions that do not shower in the ECAL leave a ionizing signal consistent with the signal a muon leaves. The shower development and energy containment for the pions is also consistent with expectations.

A subsample of pions that do not shower in the ECAL are used to study the intrinsic properties of the HCAL. We see that a small calibration correction is needed. The resolution as a function of momentum is well modeled by the expression

$$\frac{\sigma_{HC_{data}}}{E} = (20.1 \pm 2.6)\% + \frac{(62.8 \pm 11.5)\%}{\sqrt{E}} \quad (7.1)$$

A similar fit is applied to the MC sample. The simulation is seen to have too good a resolution. The simulated data require an extra amount of smearing before they can be used in an analysis to model the real data.

The full pion sample was used to measure the resolution of the ECAL and HCAL together for incident hadrons. A weighting factor was calculated to optimize the addition of the two energy measurements. The weighting factor was reasonably flat with respect to the momentum of the hadron for the real data. The Monte Carlo simulation showed a larger effect. The weighting factor is larger in both cases at low momentum, perhaps because more of the shower is contained in the ECAL at low momentum.

The combined calorimeter has a better resolution than the HCAL alone. Once again the Monte Carlo resolution is underestimated.

A previous measurement of the energy resolution of the OPAL hadronic calorimeter was done by S.Arcelli [23] and C.Y.Chang [24]. The first study with pion data in the momentum range 0 to 50  $GeV/c$  was based upon a very small sample (only 172 events), so the resolution was poorly measured in the high energy region of 30 to 50  $GeV$ . The second analysis obtained the HCAL energy resolution with a Monte Carlo pion sample in the momentum range 1 to 7  $GeV/c$ . It was found to be:

$$\frac{\sigma_{HC}}{E} \approx (21 + \frac{89}{\sqrt{E}})\% \quad (7.2)$$

It is consistent with the result measured in this thesis.

The resolutions measured in this analysis provide a better understanding of the OPAL calorimeter response to hadrons. The work here may now be applied to other analysis of OPAL data that require a detailed understanding of the energy deposited by a hadron. An example is  $\tau^- \rightarrow K^{*-} \nu_\tau$  where  $K^{*-} \rightarrow K_L^0 \pi^-$ . An analysis of this channel by the ALEPH collaboration [25] looked at the case of low momentum pions accompanied by large amounts of hadron energy; the  $K_L^0$  interacts in the calorimeters as a hadron but leaves no track to momentum analyze. The analysis depends on selecting events where the energy deposited is many times the resolution expected for the momentum of the observed pion. The work in this thesis lays the ground work for a similar analysis by the OPAL Collaboration.

# Appendix A

## The Treatment of Measurements Within Wide Bins

When a data point, measured over a bin of finite width, is to be compared to theoretical or model probability density functions,  $f$ , neither the central value of the bin nor the weighted mean value (the barycentre) of the abscissa within the bin is the appropriate place to plot the data point. Such data points should appear where the value of the predicted function is equal to its mean value over the wide bin. It is referred to as  $x_{lw}$  [26], the proper point,  $x$ , in bin of large width. The equation defining  $x_{lw}$  is

$$f(x_{lw}) = \frac{1}{\Delta x} \int_{x_1}^{x_2} f(x) dx, \quad (\text{A.1})$$

where  $f(x)$  is usually unknown and is indeed what one is trying to measure. However a theory or model may be available to predict  $f(x)$ .

In this analysis  $f$  is HCAL energy resolution,  $\sigma$ , predicted as:

$$\sigma(p) = (a + b/\sqrt{p})p \quad (\text{A.2})$$

then

$$\sigma(p_{lw}) = \frac{1}{\Delta p} \int_{p_1}^{p_2} (a + b/\sqrt{p})p dp \quad (\text{A.3})$$

where  $p$  is pion momentum.  $a$  and  $b$  are parameter which we are trying to find out in this analysis. The values of the  $p_{lw}$ , the proper track momentum, are determined by minimising the quantity at each bin

$$\chi^2 = \sum_1^N \frac{(\sigma(p_{lw}) - \sigma_m)^2}{\delta\sigma_m^2} \quad (\text{A.4})$$

where the  $\sigma_m$  is measured width of the momentum distribution,  $\delta\sigma_m$  is the error of the  $\sigma_m$ , and  $\sigma(p_{lw})$  is the predicted  $\sigma$ .

# Bibliography

- [1] The OPAL Collaboration, *The OPAL Detector at LEP*, Nucl. Instr. and Meth. **A305** (1991) 275.
- [2] The LEP Study Group, *LEP Design Report*, Vol. II, CERN LEP-TH/84-01 (1984).
- [3] G.Kane, *Modern Elementary Particle Physics*, Addison Wesley, 1987.
- [4] ALEPH Collaboration, D.Decamp, Nucl. Instr. and Meth. **A294** (1990) 121.
- [5] DELPHI Collaboration, P.Aarnio, Nucl. Instr. and Meth. **A303** (1991) 233.
- [6] L3 Collaboration, B.Adeva, Nucl. Instr. and Meth. **A289** (1990) 35.
- [7] Particle Data Group, *Review of Particle Properties*, Phys. Rev. **D 50** (1994).
- [8] O.Biebel, Nucl.Instr.Meth **A323** (1993) 34.
- [9] R.Lahmann, private communication.
- [10] A.H.Ball, *Calorimetry in the OPAL Experiment at LEP*, Beijing Calorimetry Symposium, October 1994.
- [11] H.Frauenfelder, *Subatomic Physics* (second ed.) Prentice Hall Inc. (1991).
- [12] U.Amaldi, *Fluctuations in Calorimetry Measurements*, Physica Scripta **23** (1981) 409-424.

- [13] R.Wigmans, *On the Energy Resolution of Uranium and Other Hadron Calorimeters*, Nucl. Instr. and Meth. **A259** (1987) 389-429.
- [14] R.Wigmans, *Advances in Hadron Calorimetry*, CERN-PPE-91-39, (1991).
- [15] R.Fernow, *Introduction to Experimental Particle Physics*, Cambridge University Press, (1986).
- [16] S.Weisz, D.Lellouch, *ROPE Users' Guide*, OPAL-Offline note 16/OFFL-0487.
- [17] S. Jadach, B.F.L. Ward, *KORALZ38*, Comp. Phys. Comm. **66** (1991) 276.
- [18] J. Allison, *GOPAL*, Nucl. Instr. and Meth. **A317** (1992) 47.
- [19] OPAL Collaboration, G.Alexander, *et. al.*, Z. Phys. **C52** (1991) 175.
- [20] OPAL Collaboration, R.Akers, *et. al.*, Z. Phys. **C66** (1995) 543.
- [21] OPAL Collaboration, G.Alexander, *et. al.*, Phys. Lett. **B266** (1991) 201.
- [22] OPAL Collaboration, P.Acton, *et. al.*, Phys. Lett. **B288** (1992) 373.
- [23] S.Arcelli, *A check of the hadron calorimetry calibration with pions from Tau decays*, OPAL Technical Note **TN038**.
- [24] C.Y.Chang, *et al.*, *Monte Carlo Simulation of A Gas-sampled Hadron Calorimeter*, Nucl. Instr. and Meth. **A264** (1988) 194.
- [25] ALEPH Collaboration, D. Buskulic, *et. al.*,  *$K^0$  Production in One-prong  $\tau$  decays*, Phys. Lett. **B332** (1994) 219.
- [26] G.D.Lafferty, T.R.Wyatt, *The Treatment of Measurements Within Wide Bins*, CERN-PPE/94-72, (1994).

## VITA

Surname: HU  
Place of Birth: Jilin, P.R. China

Given Names: PING

### Educational Institutions Attended:

University of Victoria	1992 - 1995
Beijing Normal University	1979 - 1983

### Degrees Awarded

B.Sc. Beijing Normal University	1983
---------------------------------	------

PARTIAL COPYRIGHT LICENSE

I hereby grant the right to lend my thesis to users of the University of Victoria Library, and to make single copies only for such users or in response to a request from the Library of any other university, or similar institution, on its behalf or for one of its users. I further agree that permission for extensive copying of this thesis for scholarly purposes may be granted by me or a member of the University designated by me. It is understood that copying or publication of this thesis for financial gain shall not be allowed without my written permission.

Title of Thesis:

A Study of the Response of the  
OPAL Calorimeter to Hadrons

Author: \_\_\_\_\_

Ping Hu

December 7, 1995